UNIVERSITY OF CALIFORNIA
RIVERSIDE

STM Study of Dynamics and Pattern Formations of Adsorbates on Cu(111)

A Dissertation submitted in partial satisfaction
of the requirements for the degree of

Doctor of Philosophy

in

Chemistry

by

Daeho Kim

June 2011

Dissertation Committee:
Dr. Ludwig Bartels, Chairperson
Dr. Chia-en Chang
Dr. Yadong Yin

The Dissertation of Daeho Kim is approved:

_____

_____

_____

Committee Chairperson

University of California, Riverside

ABSTRACT OF THE DISSERTATION

STM study of Dynamics and Pattern Formations of Adsorbates on Cu(111)

by

Daeho Kim

Doctor of Philosophy, Graduate Program in Chemistry
University of California, Riverside, June 2011
Dr. Ludwig Bartels, Chairperson

The Scanning Tunneling Microscope (STM) is well known as the best spatially resolved microscope today. Due not only to its microscopic ability, but also to its ability to manipulate individual atoms or molecules, it has been used as a very powerful tool to lead to the miniaturization of nano devices. In this study, arene molecules on Cu(111) at low temperature in ultra-high vacuum(UHV) conditions are systematically investigated using a home-built STM. By changing the size of the molecular body and functional groups, the control of their dynamics and pattern formation was successfully achieved. Density Functional Theory (DFT) calculations were also performed to support and interpret experimental results.

TABLE OF CONTENTS

CHAPTER 1

CHAPTER 2

CHAPTER 3

Chapter 1

Introduction

1.1 Scanning Tunneling Microscopy

Since the first Scanning Tunneling Microscope(STM) was invented by Gerd Binnig and Heinrich Rohrer in 1981,[1] it opened a new world to the field of microscopy by being able to image and manipulate individual atoms and molecules. Also, by adding ultra-high-vacuum and low-temperature features, site-specific vibrational spectroscopy of adsorbates was made possible.[2]

The principle of a STM is based on the quantum mechanical phenomenon called tunneling. In classical mechanics, when a particle tunnels through a barrier, it needs higher kinetic energy than the potential energy. However, in quantum mechanics, the tunneling process is possible with a certain probability even though the kinetic energy is lower than the barrier energy. Since this quantum mechanical tunneling process is only possible at an extremely small scale, and it's very sensitive to the distance between two conducting materials, it has allowed the STM to have atomic spatial resolution. This tunneling process can be understood by the simplified formula.

$$I \propto e^{-kd} \quad \text{where } k=\sqrt{\frac{2m\Phi}{\hbar^2}} \qquad \text{Eq.1}$$

With a typical value of work function of metals, the calculated k value is ~2.2Å^{-1} and d is a distance between the STM tip and surface. 1Å of distance change gives an almost of one order of magnitude of the current change.

1.2 STMs in Bartels Group

Three STMs were used to perform the experiments of this study. Two of them have bath cryostats and the other a flow cryostat. Each system has its own advantages and disadvantages. Bath cryostat STMs have better vibration isolation due to the absence of a cryogenic liquid(LN_2 or LHe) transfer line from the dewar and noise of flow. Another main advantage of the bath cryostats is the high efficiency of liquid helium consumption. Compared to flow cryostat systems, their liquid helium consumption is 50% smaller when the system stays at its lowest temperature (~10K).

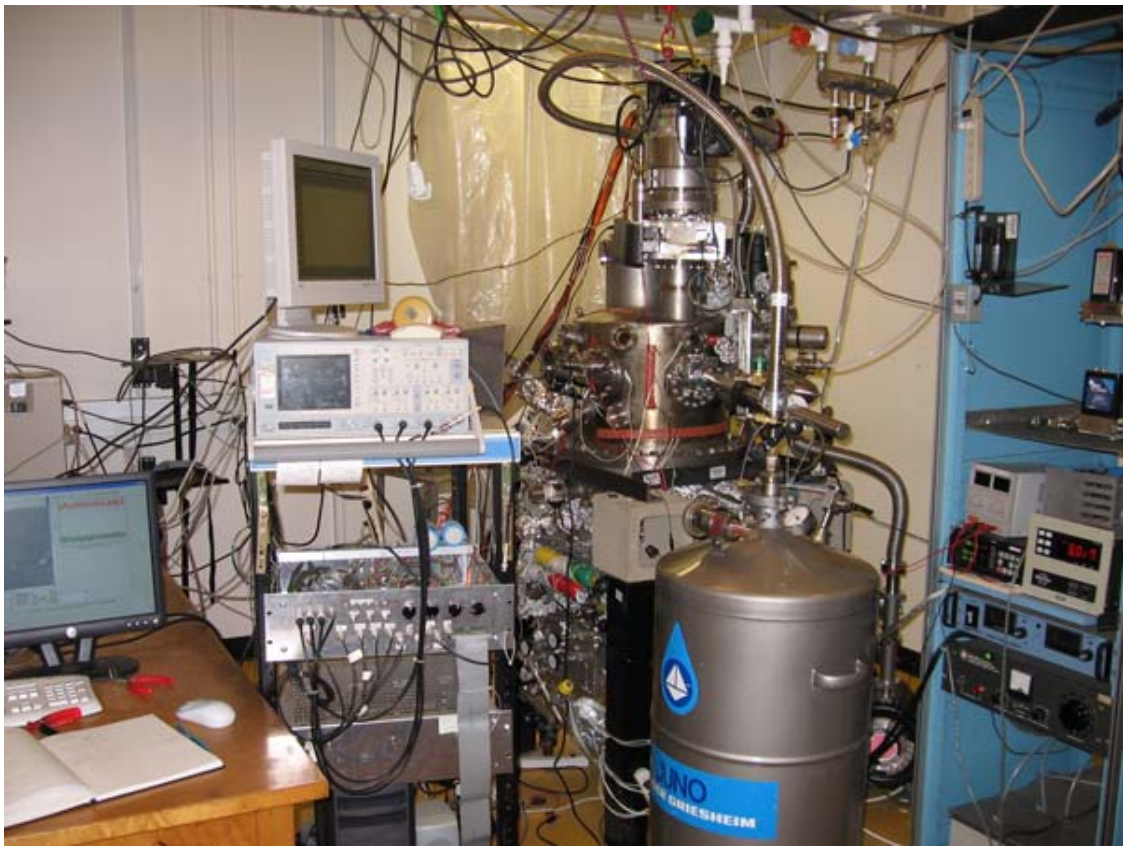

Figure 1.1 A flow cryostat STM.[3]

On the other hand, the flow cryostat has an ability to image up to four days with a regular 100L liquid helium dewar at its lowest temperature without halting the imaging process. For the study of atom or molecule dynamics, it is very critical to have enough time for continuous monitoring, sometimes for more than a week. Additionally, temperature control is easily done by controlling the flow of cryogenic liquid. These features are not available in the bath cryostat systems. The temperature can be controlled in the bath cryostat system by providing a heat source near the scanning unit but it increases the temperature from the intrinsic low temperature of cryogenic liquid, therefore it lacks the efficiency of insulation that the bath cryostat has.

Each system is a UHV chamber consisting of a sample preparation area with a sputter gun, molecule dosing setup, wobble stick access to the cryostat door and STM spring mechanisms, turbo pump, ion pump and titanium sublimation pump. One of the bath cryostat systems has a metal evaporator and a gate valve between a prep chamber and an STM chamber. In addition, a flow cryostat system has multiple tip holders, which allow in situ tip change without breaking the vacuum.

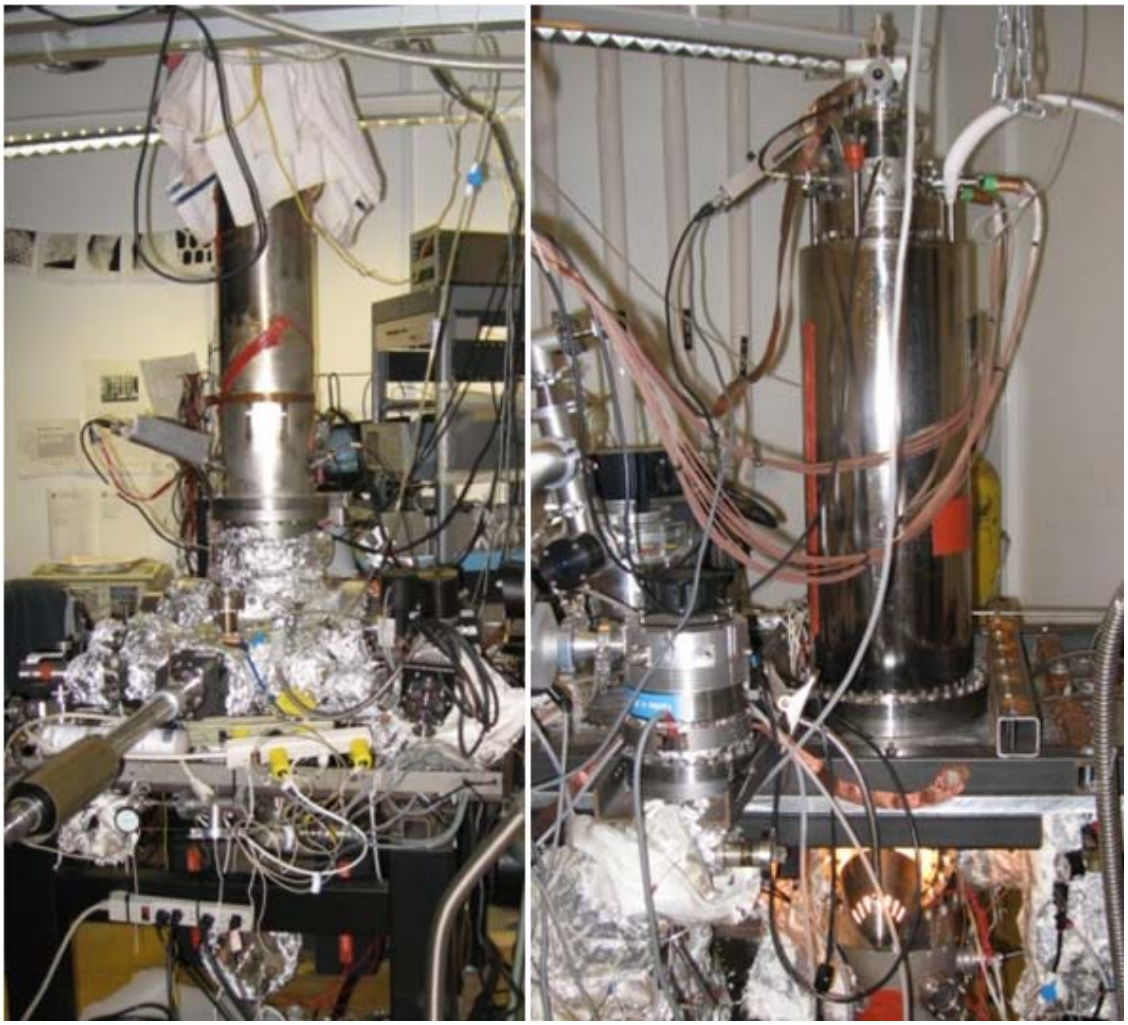

Figure 1.2 Two bath cryostat STMs in Bartels group.

1.3 Experimental

In this study, only a Cu(111) single crystal was used as substrates. A copper crystal has a face-centered-cubic unit cell with a lattice constant of 2.55Å. The (111) surface is the most thermodynamically stable. The crystal is cleaned by a cycle of sputtering and annealing. Sputtering consists of a 3kV ion accelerating electric field combined with 20mA of filament current to produce thermal electrons that will ionize Ar to Ar^+ at $2x10^{-5}$torr of Ar backfilling pressure. With this sputtering setup approximately 6uA of current was measured from the sample to the ground. For annealing, a coil of tungsten wire, 0.006" in diameter, and of approximately 6cm wire length, was used as a contact resistive heating method. With this filament, a total power of 20W was set with ~1.4A of current and ~15V of voltage and annealed for 20 minutes. Using this setup, the temperature of the Cu(111) single crystal sample can reach up to 500ºC, at which point copper begins to glow as ascertained by visual inspection. At this temperature, surface melting can occur and surface copper atoms rearrange to form large terraces. After six or more sputtering and annealing cycles, the cleanliness of the sample was confirmed by STM scanning at room temperature and cryogenic temperature. Figure 1.3 shows an STM image of a clean Cu(111) single crystal sample.

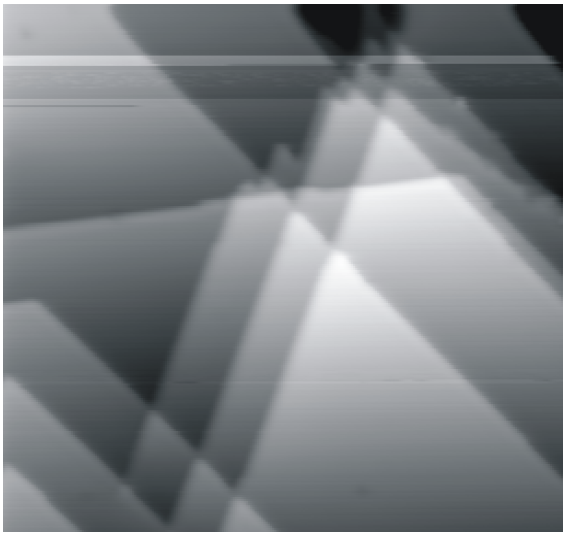

Figure 1.3 A clean Cu(111) surface (52nm × 52nm).[4]

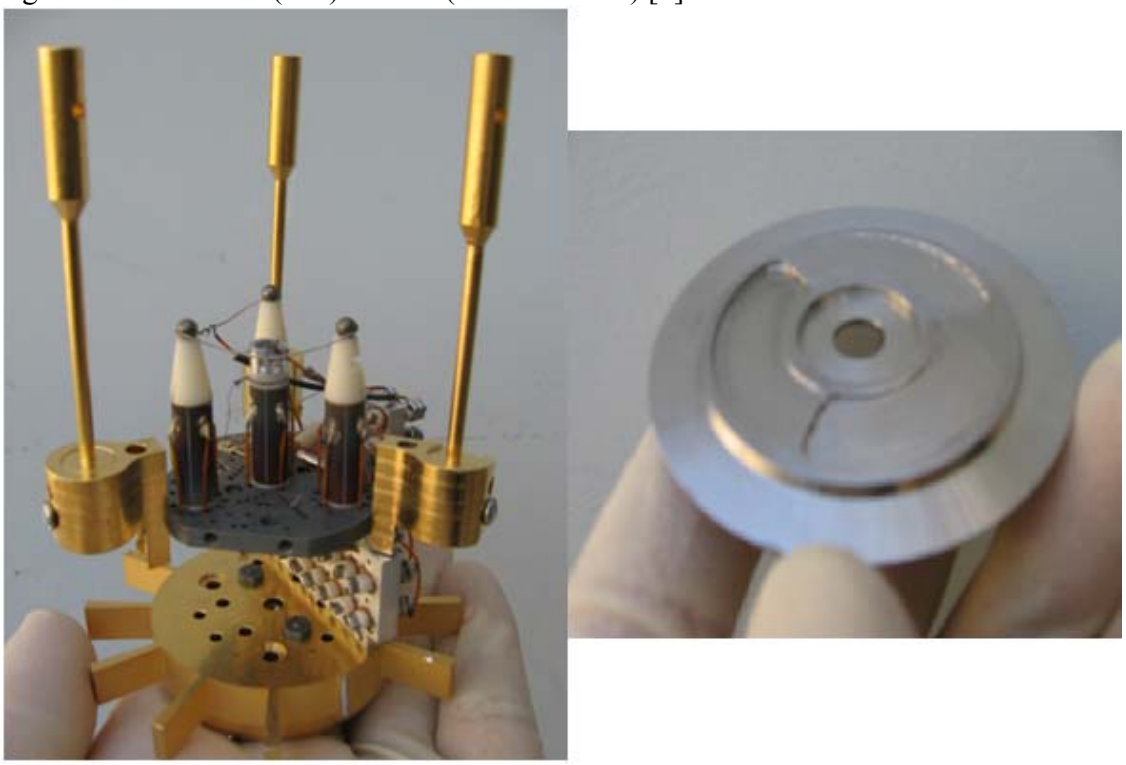

Figure 1.4 Scanning unit(left) and a ramp(right).

Fig. 1.4 shows a scanning unit and a ramp. There are three outer piezoelectric tubes for the coarse movements of the x and y axes and one center piezo for the fine z-axis movement. On the top of each outer piezoelectric tube, a well polished metal ball is positioned to give slip-stick motions to the ramp so that it can move vertically. On the top of the center piezoelectric tube, the tungsten tip is positioned. While scanning, three outer piezoelectric tubes give x- and y-axis movements, and the center piezoelectric tube independently moves only in the z direction to continuously be adjusted to maintain a constant tunneling current.

1.3.1 Deposition of Molecules

The deposition method of molecules onto the Cu(111) surface can be categorized in two ways: one way for solid molecules, and another for liquid molecules. For solid molecules, a differentially pumped small chamber is prepared and mounted to the prep chamber with a gate valve so that it can be separately prepared without breaking the vacuum of the prep chamber. After dosing, the chamber pressure reaches back to 10^{-10} torr range by differential pumping, the gate valve is opened, and the mass spectrometer is used. While the mass spectrometer is monitoring the masses of the dosed molecules and their fragments, the solid sample in the glass capillary tube is heated. The desired heating temperature of the molecules depends on their vapor pressure and decomposition temperature. Once the main molecular mass peak appears on the mass spectrum, the dosing time is determined by the peak intensity on the mass spectrometer as well as the total pressure. This process is actually performed twice; first a test dose determines the

preferred dosing conditions, and then the real dosing is performed after pressure goes back to a base pressure in the 10^{-10} torr range. For real dosing, the Cu(111) sample is positioned at the line of sight from the molecule sample. Then the dosing process is conducted with parameters determined by the dummy dose. For a liquid sample dosing setup, most of the procedures are the same as the solid molecule dosing setup. Since liquid molecule samples usually have a high enough vapor pressure usually more than 10^{-9} torr at room temperature, the heating process is not necessary. Instead, the precision leak valve is needed to decrease the dosing pressure. Aditionally, a freeze-pump-thaw process is required to get rid of solvent impurities. Except for these additional processes, all other procedures are the same as in the solid molecule dosing setup. Usually this dosing process is conducted when the copper sample is at cryogenic temperature so that the sticking coefficient is higher than what it would be at room temperature. After dosing, the copper crystal is usually annealed to a room temperature to 700K, depending on molecules, so that the molecules have sufficient energy to move about the surface and form a self-assembled structure – the temperature at which this occurs depends on the properties of the dosed molecules. Once the sample has been prepared according to this dosing process, the sample is scanned to confirm the coverage, and if it is too low or high another dosing process is repeated with adjusted parameters until the preferred coverage is observed.

1.3.2 Density Functional Theory Simulations

Density functional theory (DFT) calculations are used to determine the electronic structure, molecular geometries, and binding energies of the species of interest at various adsites. All DFT calculations were performed using the Vienna Ab Initio Simulation Package (VASP)[5] implementing the generalized gradient approximation (GGA) for the exchange-correlation functional[6] and the plane-wave pseudopotential method.[7] By combining the results of these calculations with our experimental data it is possible to get a more complete picture of the fundamental interactions and processes taking place in these systems. The detailed setup for each simulation will be addressed in the corresponding chapter.

1.4 Thesis Overview

In chapter 2, the network formation based on metal coordination bonding with 9,10-anthracene-dicarbonitrile(DCA) will be discussed. This result shows a facile way to prepare patterns using organic-metal coordination bonds compared to the conventional two step method.[8] Also, theoretical calculations show the presence of an anionic character to the metal adatoms, which could be an application for heterogeneous catalysis.

In chapter 3, pattern formation by a particular class of arenethiol molecules will be discussed. Coworkers and I investigated how the optimization of the intermolecular interactions of a hydrogen atom at one particular position on the specific arene system leads the prediction of pattern formation of this molecular system. This may provide a general guiding principle for the design of arenethiol films.

In chapter 4, it will be shown that the molecular walkers, molecules that are capable of moving unidirectionally across a substrate violating its symmetry, can be tuned over a wide range by utilizing extension of their aromatic backbone, insertion of a second set of substrate linkers (converting bipedal into quadrupedal species), and substitution on the ring. Aditionally, density functional theory simulation of the molecular dynamics identifies the motion of the quadrupedal species as pacing (as opposed to trotting or gliding). Knowledge about the diffusion mode allows us to draw conclusions on the relevance of tunneling to the surface diffusion of polyatomic organic molecules.

In chapters 5 and 6, nanoscale confinement of adsorbed CO molecules in an anthraquinone network on Cu(111) with a pore size of 4 nm will be discussed. In contrast to extended terraces, confinement allows correlation between adsorbate diffusivity and the number of adsorbates in the pore. Also, molecules occupy the states approximately in the sequence of rising electron energy. In combination, coworkers and I found that in confinement, CO molecules are much more likely to be at adsorption sites that allow lateral access, in contrast to the dense and uniform films on extended terraces.

In chapter 7, the compression of the anthracene film in terms of continuum elastic properties is estimated. Adsorbing anthracene on a Cu(111) surface results in a wide range of complex and intriguing superstructures spanning a coverage range from 1 per 17

to 1 per 15 substrate atoms. In combination with the first-principles density-functional theory calculations, coworkers and I show the essential role of van der Waals interactions in estimating the variation in anthracene adsorption energy and height across the sample.

Finally, in chapter 8, a sulfur pre-loaded Cu(111) surface with a separate deposition of molybdenum will be discussed. The resultant film morphology as a function of the sulfur pre-loading of the substrate will be shown. Also, benzenethiol was used as a sulfur source; it is not commonly used for this purpose. The formation of molybdenum disulfide of different geometry and layer thickness was observed depending on the sulfur decorations of the substrate.

Chapter 2

Spontaneous metal coordination bonding on Cu(111)

(From publication: Angewandte Chemie International Edition 2008, 47, 8442-8445)

2.1 Introduction

In the quest for increased control and tunability of organic patterns at metal surfaces, more and more system emerge that rely upon coordination of metal adatoms by organic ligands using endgroups such as carbonitriles, amines and carboxylic acids.[9-19] Such systems promise great flexibility in the size and geometry of the film pattern through choice of the ligand body, the number and arrangement of ligating endgroups and the nature of the metal centers. Planar (trigonal or square) arrangements of ligands around metal centers are observed most commonly as a result of attractive interactions of the ligands with the substrate. In contrast, in the solution phase planar, and in particular trigonal planar, arrangements are quite rare and generally require ligands whose nature (e.g. bidentate, pincer shape) forces planarity.

Given the relative immaturity of the field of surface coordination chemistry compared to its solution-phase counterpart, it would be of great interest to know, which information can be gleaned from the latter to predict that for the former. Aspects of coordination

chemistry at surfaces that have attracted very little attention so far are the effective oxidation state of the metal atom, which is much more straight-forward to define in the solution phase, and the response of the coordination center to the presence of ligands at a surface.[20] This study details an effort at gaining some insight into these two aspects using a coordination system, which is particularly facile to prepare, as it relies on substrate atoms as coordination centers rather than requiring their separate deposition. In particular, this study describes the formation of a hexagonal network out of 9,10-anthracene-dicarbonitrile(DCA, Fig. 2.1) on Cu(111) by titration of a nearly square molecular arrangement with copper atoms released by annealing from the substrate. Coworkers and I apply a combination of experimental and theoretical methods and juxtapose their results with the molecular patterns in the absence of a substrate. Individual DCA molecules adsorb flat onto Cu(111) with the anthracene moiety parallel to the high-symmetry direction of the substrate.

2.2 Experimental

A home-built variable-temperature scanning tunneling microscope (STM) operated in ultra-high vacuum was used for the measurement. Cu(111) sample preparation involved sputtering (Ar+, 3 kV) and annealing of a single crystal followed by cooling to liquid nitrogen temperatures within the STM. Deposition onto the cold sample occurred from a glass capillary attached to the vacuum chamber through a gate valve in a line-of-sight fashion while controlling the deposition rate through measurement of the pressure in the

vacuum chamber. Density functional theory calculations of the electronic and geometric structures and adsorption energies of DCA on Cu(111) were carried out using the Vienna Ab Initio Simulation Package (VASP)[5] implementing the generalized gradient approximation (GGA) for the exchange-correlation functional[6] and the plane-wave pseudopotential method.[7] Projector-augmented wave (PAW)[21] pseudopotentials were used for all atoms in the system. The cutoff energy for the plane-wave expansion is taken to be 400 eV and, depending on the unit cell size, a 2x2x1 Monkhorst-Pack k-point mesh or a single point are used in Brillouin zone sampling[22] to obtain converged results for the total energy of the system. Coworkers and I typically restricted our calculation super cell to two or three substrate (copper) layers so as to keep the total number of substrate atoms in the supercell to approximately 100 for computational feasibility. During lattice relaxation, all adsorbate and top-layer substrate atoms were allowed to move in all directions. The structures and energies that are shown in this study result from relaxation of the forces acting on each atom to better than 0.01 $eVÅ^{-1}$. The physisorbed adsorption energy of DCA is approx. 0.4 eV. Coworkers and I wish to caution, however, that GGA occasionally underestimates the absolute binding energy in physisorbed systems.[23]

2.3 Results

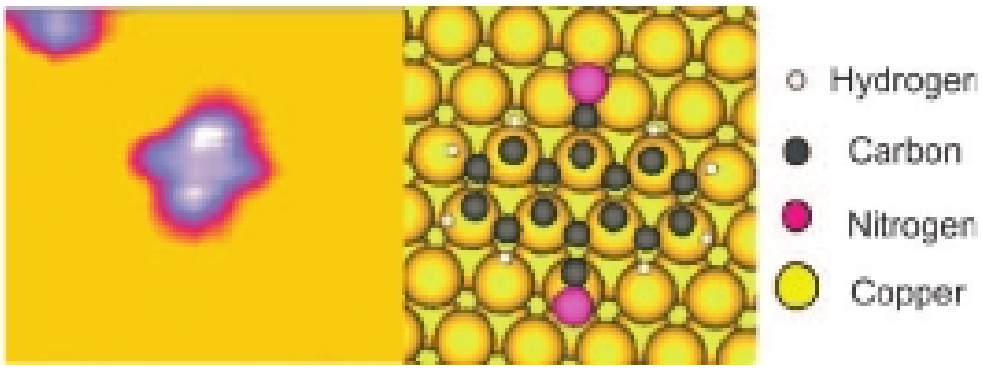

Figure 2.1 Left: STM image obtained at 25 K (35x30Å, -1.9 V, 0.046 nA). Right: calculated adsorption geometry of DCA.

Individual DCA molecules adsorbs flat on Cu(111) with the anthracene moiety parallel to the substrate high-symmetry direction. Fig. 2.1 shows an STM image of DCA on Cu(111) and the simulation of the adsite using DFT on a 5x5x3 substrate atoms. While the adsite of DCA resembles that of its oxygen[24] and sulfur[25] counterparts (anthraquinone and 9,10-dithioanthracene, respectively), DCA does not diffuse in an uniaxial fashion on Cu(111) and it also does not show more facile lateral manipulation along any particular substrate directions. Even at 90K DCA retains sufficient surface mobility to assemble in patterns or to reach step edges.

Increase of the DCA coverage initially leads to the formation of molecular rows followed by the formation of an ordered array of molecules featuring a nearly square unit cell, that is described in matrix notation as $\begin{pmatrix} 3 & 3 \\ -1 & 4 \end{pmatrix}$ (see left of Fig. 2.2.a and Fig. 2.2.b).

Each unit vector of this adsorbate pattern is 9.2 Å long and the angle between them is 88^{o} for a total of 15 substrate atoms per adsorbate. In this arrangement, all DCA molecules lie with the anthracene moiety in parallel and successive rows of molecules are in antiphase bringing the nitrogen atoms of one row of molecules close to the terminal hydrogens (i.e. positions 2, 3, 6, 7) of two neighboring molecules (Fig. 2.2 d). In this study, this pattern will be referred to as the α phase.

Recently, it is shown that hydrogen bonds of oxygen or sulfur atoms with terminal hydrogen atoms of anthracene derivates on Cu(111) are associated with bond energies of 20-50 meV[26] and bond distances of C-H···O of 2.8 Å.[27] In the DCA case, the C-H···N distance is somewhat longer at 3.1Å and yet each N atom is involved in two hydrogen bonds (in contrast to one bond for the previously addressed case). To verify the presence of an attractive interaction between the nitrogen and the hydrogen atoms, DFT calculations were performed in which two molecules were placed on a 5x9x3 substrate atoms unit cell so that they either formed two adjacent rows of molecules separated by empty space from the next double row, or so that they formed separated rows thus allowing for hydrogen bonding in the first but not in the second case. The first case has the lower total energy by 26meV, indicating a hydrogen bond-energy of 0.01eV, which is very small but reasonable for the system investigated.[28] Coworkers and I also find that in the case of adjacent rows the bonds are elongated by approximately 5pm towards their

hydrogen bond partners, as compared to the case of separated rows, in further support of a local attractive interaction.

While previously reported metal coordination networks at surfaces generally require a separate deposition step for the coordinating atoms, DCA/Cu(111) is more facile in its preparation: continuously increasing the sample temperature at a rate of approx. 5K per hour starting from 90K, the formation of a new pattern was observed at approx. 180K. At this temperature a small amount of substrate atoms form a 2D copper adatom gas that can interact with the DCA molecules[29] and form a coordination pattern. The amount of copper adatoms available for coordination then depends experimentally only on the temperature (and duration) of the anneal. Fig. 2.2a shows a sample at 180K which besides the α phase also features a DCA/Cu pattern on the right (β phase). This pattern incorporates one copper adatom for every three DCA molecules; each DCA molecule is coordinated with copper only on one side, with the opposite nitrogen terminal free to form hydrogen bonds similar to the copper-adatom-free case. Each copper atom is coordinated by three DCA molecules in a trigonal planar arrangement. The resultant unit cell is (√48x√48)R30° with 48 substrate atoms, 3 molecules and one adatom per unit cell. It is noteworthy that the annealing procedure leads to an adsorbate pattern on the surface that is less dense than the original pattern (one DCA per 16 substrate atoms, as opposed to one DCA per 15 substrate atoms for the α phase).

Coworkers and I calculated the total energy of 6x8x2 substrate atom supercells for the following cases: without any adsorbate, with a single Cu adatom, with the three DCA molecules in a trimer arrangement and with the DCA molecules and the coordinated Cu adatom. Comparison of the values shows that coordination provides a net binding energy of almost 1 eV (or 330 meV per Cu-N bond), substantially in excess of the energy of the hydrogen bonds lost. A close inspection of the adposition of the coordinated molecules shows, that the N···H-C bond length increased substantially as a result of metal coordination of the opposite nitrogen (compare Fig. 2.2.d and Fig. 2.2.f). The inability of metal-coordinated DCA molecules of participating in a hydrogen-bonded network explains the separation of the adsorbate population into islands of metal coordinated molecules and those consisting of pure DCA - despite the fact, that these islands have a commensurate edge (see Fig. 2.2.a). Fig. 2.2.a also shows that the molecules are locked in place much more securely in the β phase, while the fuzzy edge of the α phase attests to constant attaching and detaching of molecules from this side of the island thereby contributing to a lattice gas of admolecules and adatoms that lets the β phase grow.

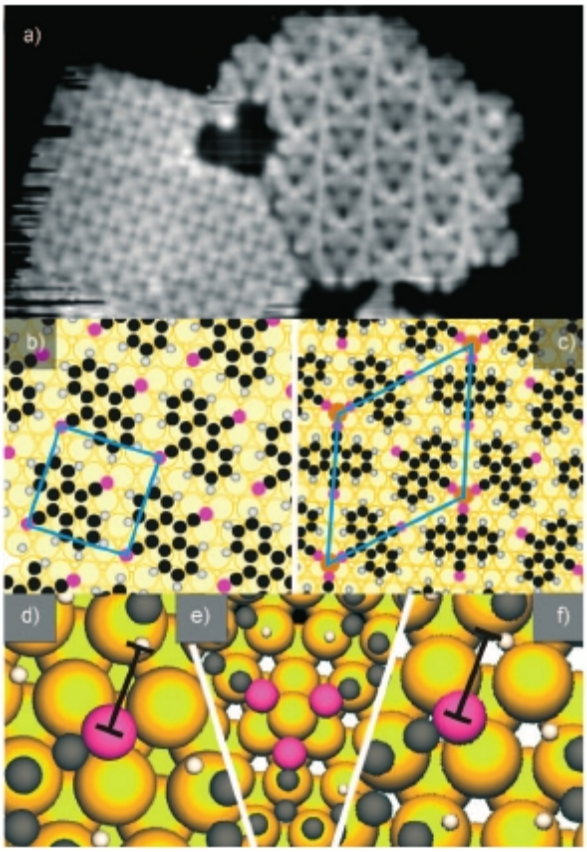

Figure 2.2 a) STM image of DCA on Cu(111) obtained at 180 K (175x95Å, -2.6V, 0.22 nA), depicting separate regions of the α phase (left) and β phase (right). b),c) DFT minimization of the adsorbate patterns (α and β phase) with the unit cell indicated. Because the unit cell in (c) is more than three times larger, only two substrate layers were included. d) Hydrogen bonding in the α phase. e) Coordination of a Cu adatom in the β phase. f) Increased N···H-C length in the β phase indicating the absence of hydrogen bonding. The calculations for the α and β phases used two and three substrate layers, respectively, leading to the difference in apparent background of panels (d), (e), and (f). Key as for Figure 2.1.

Titration of all nitrilo groups of the available DCA molecules with Cu atoms from the substrate by means of annealing to room temperature for 100 minutes leads to the formation of a film in which both nitrilo groups of DCA coordinate with copper atoms (γ phase). Fig. 2.3 shows an STM image and a model of this molecular arrangement. Its 7x7

unit cell encompasses 49 substrate atoms, three DCA molecules and 2 adatoms, one of which occupies an hcp site and the other an fcc site. The adsorption geometry of DCA resembles closely that of the previous two patterns. Notably, the DCA density on the substrate is further reduced, causing the STM image to reveal a pattern that resembles a honeycomb with apparently empty space surrounded by the DCA molecules.

While the evolution from a hydrogen-bonded to an atom-coordination based network is readily explained by the associated binding energies, the reason for the transition from a nearly square to a trigonal network is not immediately apparent. While the sixfold symmetry of the substrate may favor a trigonal setup, there is no reason why the coordination-based pattern should reflect the substrate symmetry any more (or less) than the hydrogen-bonded one.

In contrast to surfaces, there is abundant data available on the coordination chemistry of metal atoms (including copper atoms and cations) in the solution phase, yet no copper-DCA complexes have been reported to the knowledge of the authors. A statistical analysis of crystal structures[30] shows that Cu complexes have an oxidation state distribution of 38% Cu^{1+} and 62% Cu^{2+}. Of all complexes, only 13.8% are trigonal planar; 93% of these being the more reduced Cu^{1+}. Except for cyanocuprate(I) networks,[31] trigonal planar configurations occur only in the presence of bidentate ligands. Although DCA is not a bidentate ligand in this sense, it may still be illustrative to

explore, whether the coordination geometry of Cu adatoms at surfaces should resemble that of a monovalent cation in the solution phase, or whether closer resemblance to other oxidation states is found.

Relaxation of an uncoordinated Cu adatom on top of the 6x8x2 substrate unit cell in the context of the previously mentioned calculations produces an inward relaxation of 0.2Å, which is similar to that found in other calculations.[32] Unsuprisingly, integration of the charge density around the copper adatom over the Wigner Seitz cell surrounding it results in the same amount of charge found surrounding other surface atoms. However, in the case of a Cu adatom coordinated by three DCA molecule no inward relaxation is found and integration of the charge density leads to an excess of one electron, even after subtracting the charge density of the neighboring nitrogen atoms (found by calculating the charge density for the same fixed surface and adsorbate setup without the copper adatom present). While the extra charge density at the copper adatom justifies the lack of inward relaxation, it is initially counterintuitive to the behavior generally expected of adatoms. It should by no means be interpreted as the copper atom withdrawing charge from DCA molecules; rather the Cu adatom appears to serve as a conduit allowing the DCA nitrogen atoms to interact effectively with the substrate electron density. In the course of this interaction, the adatom donates charge to the coordination bonds with the three nitrogen atoms. Given the size of the Wigner Seitz cell, which is based on the 2.55Å Cu-Cu distance in the bulk, in comparison to the shorter Cu-N spacing (of 1.65Å

in the surface plane, 1.99Å along the Cu-N vector) this charge remains, at least partially, in the Wigner Seitz cell and it is part of the integration. The Cu adatom is at no point uncoordinated and negatively charged. However, in establishing the coordination bonds it obtains approx. 1 charge from the substrate so that it can serve as a donor to each of its ligands of approx. 1/3 charge without becoming itself positively charged. Solely in this characteristic it resembles an anion. As negatively charged Cu centers are generally not observed in the solution phase, for comparison the lowest energy conformation of free Cu^{x}(dicyanobenzene)$_3$ complexes was computed with x=-1, 0, +1 using (HF/3-21G*) in Spartan 06.[33] While a trigonal planar configuration is stable for all copper oxidation states, coplanar arrangement of the ligands aromatic moieties is stable exclusively for x= -1, for which the Cu-N bonds are the shortest and, not surprisingly, strongest, in further support of the favorite character of the configuration observed at Cu(111).

Fig. 2.4 shows on the left a top and a side view of the charge density surrounding an adatom in the β phase. The right side shows the excess (red) and missing (blue) charge density compared to the same fixed surface setup after artificial removal of the Cu adatom. The high charge density at the location of the adatom is apparent, and also the donating character of the substrate (bottom right). Note the decrease of charge density immediately next to the nitrogen atom due to the conversion of its lone pair into a coordinating one, the reduced charge density at the C≡N bond and the emerging π bond of the nitrilo group to the ring system, converting the original C≡N-Anthracene setup

partially towards a Cu-N=C=Anthracene sequence in further support of the profound dative impact of the N-Cu coordination on the charge density in the molecule.

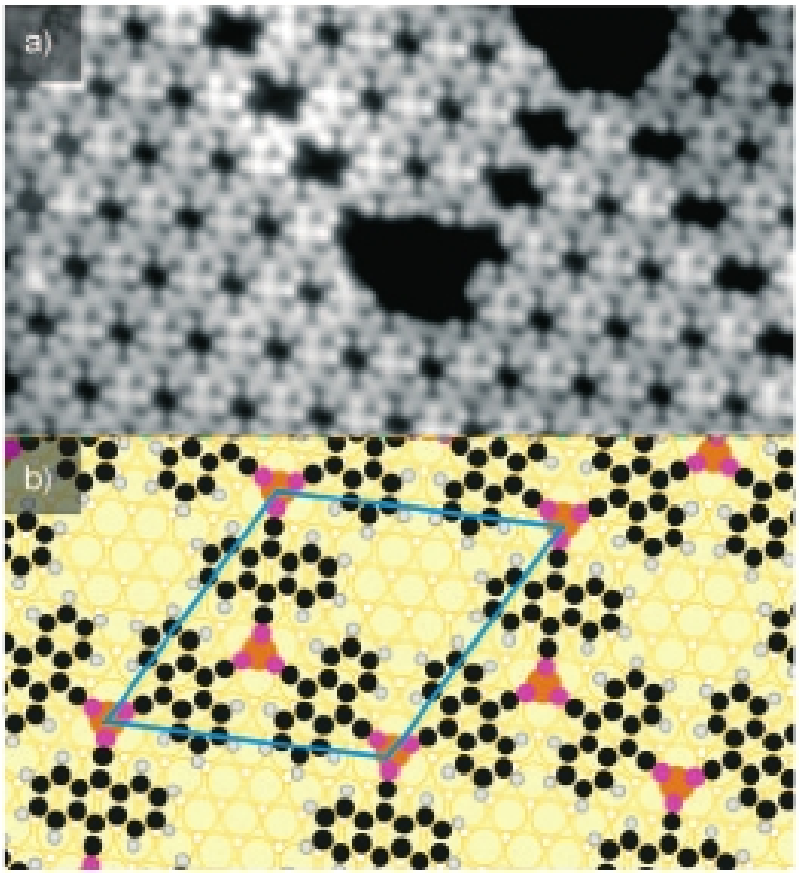

Figure 2.3 a) STM image (180x100Å, -3.8 V, 57 pA, 30 K) of the γ phase of DCA on Cu(111). b) Corresponding model. Key as for Figure 2.1.

2.4 Conclusion

Coworkers and I presented a coordination network, formed at a metal surface in a system facile to prepare because the required metal centers can be released in a measured fashion from the substrate by simple annealing. Analysis of the charge density in this system

suggests that metal adatoms can have a pronounced donating character despite the electron deficiency of uncoordinated adatoms. The notion that metal adatoms present an anionic character in their interaction with molecular adsorbates could have significant and widespread implications (for example, in heterogeneous catalysis). For instance, the concept that negative charging is at the origin of the high activity of gold nanoparticles in CO oxidation is already a topic of discussion.[34, 35] Further examples of this behavior need to be found before any generalizations can be made.

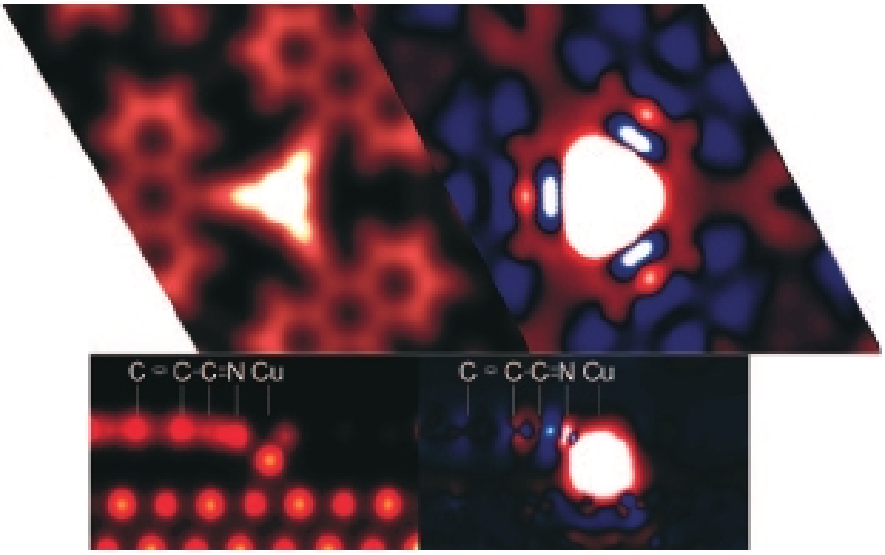

Figure 2.4 Left: charge density around a copper adatom coordinated by three DCA molecules seen from parallel (top) and perpendicular (bottom) to the Cu(111) plane. Right: changes in charge density after artificial removal of the Cu adatom (excess charge shown in red, deficit in blue). Charge transfer from the substrate and partial conversion of the cyano triple bond into a double bond, and of the CÀC single bond to a double bond is apparent.

Chapter 3

H-atom position as a pattern determining factor in arenthiol film

(From publication: Journal of American Chemical Society, 2009, 131, 5540–5545)

3.1 Introduction

The conducting and dynamic properties of (thiolated) arenes on coinage metal surfaces have been studied intensely because these compounds feature both outstanding facility in the fabrication of molecular scale contacts (i)[36, 37] and unique diffusive properties (ii).[25] Arenes stacked parallel to the surface have been suggested for charge injection at metal electrodes (iii).[38] While for application (i) the molecule is generally lifted at least partially from the substrate and the interaction of the thiol group with the substrate is paramount, (ii) relies on a delicate interplay between sulfur and arene substrate interactions and (iii), for which generally unthiolated arenes are used, crucially depends on the arene-substrate interaction and ensuing columnar stacking pattern. Despite these technological promises there have only been very few studies addressing pattern formation in such films in a systematic fashion, ie. addressing more than 1 or 2 related compounds. While many interesting phenomena have been observed already, generally not a sufficient number of related molecules were investigated to glean general

rules. In contrast, pattern formation of alkanethiols on coinage metal surfaces (in particular gold) has been addressed extensively, mainly because those systems provide a convenient path for self-assembled functionalization.[39, 40]

Intermolecular hydrogen bonds have emerged as important pattern-determining factors,[41-53] even for systems in which conventional X-H···X' bonding (with X,X' = O,N,F) cannot occur.[26, 27, 54-56] They provide an alternative to pattern control by means of substrate reconstruction,[57] electrostatic interaction[58, 59] or surface coordination chemistry,[13] yet there is no comprehensive understanding, which hydrogen atoms feature most prominently in them. Hydrogen bonding is known to depend delicately on the electronic structure, bond length and bond angle, a problem reappearing in many current disciplines of chemistry from surface science to proteomics.

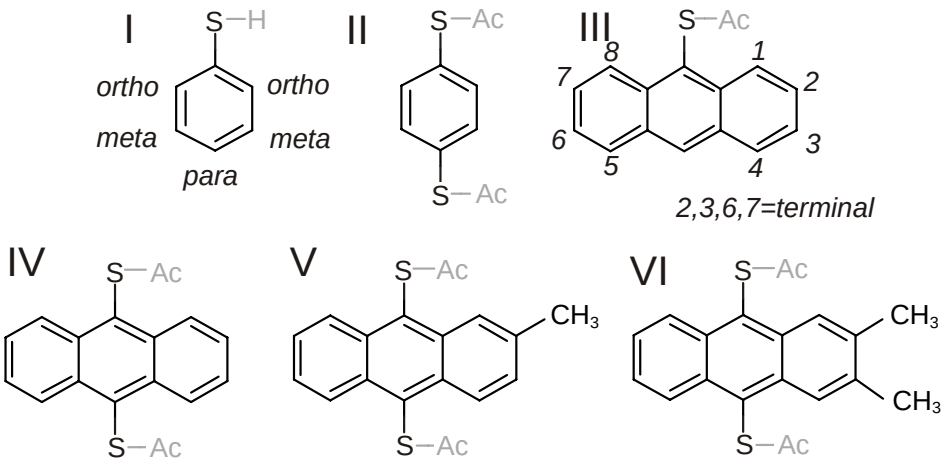

Scheme 3.1 BT (I), BDT (II), AT (III), ADT (IV), MADT (V), DMADT (VI)

In this study Coworkers and I contrast the pattern formation (or the absence thereof) in coverages of benzenethiol (I, BT), benzene-1,4-dithiol (II, BDT), anthracene-9-thiol (III, AT), anthracene-9,10-dithiol (IV, ADT),[25] 2-methylanthracene-9,10-dithiol (V, MADT) and 2,3-dimethylanthracene-9,10-dithiol (VI, DMADT) adsorbed on Cu(111). These experiments were performed in ultra-high vacuum and use scanning tunneling microscopy at cryogenic temperatures.

3.2 Experimental

3.2.1 Imaging

A home-built variable-temperature scanning tunneling microscope (STM) operated in ultra-high vacuum was used for the measurement. Cu(111) sample preparation involved sputtering (Ar^+, 3kV) and annealing of a single crystal followed by cooling to liquid nitrogen temperatures within the STM. Deposition onto the cold sample occurred for anthracene-based species from a glass capillary attached to the vacuum chamber through a gate valve in a line-of-sight fashion while controlling the deposition rate through measurement of the pressure in the vacuum chamber. Benzene-based species were dosed through a needle valve due to their higher vapor pressure. BDT and all anthracene-based species were acetyl protected prior to deposition (see Synthetic section below) and required post-deposition anneal of the sample to room temperature in order to remove protecting groups, which was confirmed by mass-spectrometry.

3.2.2 Theoretical Calculations

Density functional theory (DFT) calculations of the electronic and geometric structures and interaction energies of all molecules on Cu(111) were carried out using the Vienna Ab-Initio Simulation Package (VASP)[60] implementing the generalized gradient approximation (GGA) for the exchange-correlation functional[6] and the plane-wave pseudopotential method.[61] Ultrasoft pseudopotentials[21] were used for all atoms in the system. The cutoff energy for the plane-wave expansion is taken to be 400 eV and a single k point is used in Brillouin zone sampling to obtain converged results for the total energy of the system. All supercells have three substrate (Cu) layers so as to keep the total number of substrate atoms in the supercell to approx. 100 for computational feasibility. During lattice relaxation, all adsorbate and top-layer substrate atoms were allowed to move in all directions. The structures and free energies that are shown in this study result from relaxation of the forces acting on each atom to better than 0.02 eV/Å. Calculations of the molecular structure in the gas phase use BLYP/6-31G* in Spartan.[33]

3.2.3 Synthetic

The synthesis of AT, MADT and DMADT follows the synthesis of 9,10-dithioacethylanthracene described in Ref. [25]. Coworkers and I used appropriate oxygen based precursors and converted them with Lawesson's reagent to the polymerized or dimerized anthracenedisulfide, whose sulfur atoms subsequently esterfied via reduction

with sodium borohydride followed by in situ addition of acetic anhydride. BDT was obtained from Alfa Aesar and it is acetyl-protected to avoid polymerization during deposition.

All reactions were carried out under N_2 and Ar gas and all glassware was dried in an oven at 100 ^{o}C. All solvents (HPLC grade) were used without purification. The reactions were identified by thin layer chromatography using UV light. The compounds were purified by column chromatography (particle size 230-400 mesh).

3.3 Results

3.3.1 Benzene Derivates

The Yates' group showed that BT is capable of extracting atoms from a gold surface to form BT-Au-BT bridges similar to those on gold nanoparticles.[62, 63] BT adsorbs on Cu(111) under hydrogen abstraction (at temperatures as low as 40K)[64] with its sulfur anchor close to a substrate bridge site, i.e. without extraction of a substrate atom. BT has a diffusion barrier of 150 meV and it is able to rotate at 120-130 meV barrier through two sets of three equivalent adsites with slightly different binding energies (see Fig. 3.1a).[65]

In this study coworkers and I followed the evolution of a number of BT molecules while increasing the substrate temperature from 50-90 K (i.e. by ≈ 70%). By scanning same

area for long time, a movie was obtained showing >700 continuous images from this series acquired over >24h. Initially, a number of odd-shaped molecular aggregates, isolated molecules (yellow in Fig. 3.1c), dimers (red), trimers and tetramers were observed. Unsurprisingly, isolated molecules become mobile first and attach to nearby islands. Subsequently, dimers become mobile and start to rearrange. Analysis of a large number of STM images at high resolution and ≈ 60 K temperature reveals the distribution of dimers shown in Fig. 3.2c. The majority of dimers are found to interact by placing the sulfur atom of one molecule in the vicinity of an H_{ortho} of another molecule. In most cases (purple portion) both molecules adsorb in the preferred adsorption configuration (left in Fig. 3.1a), yet in some cases at least one of the molecules occupies the less favored one (yellow portion). A significantly smaller number of molecules are found to interact via the H_{meta} and even fewer via H_{para}.

DFT calculations were performed, in which coworkers and I placed two BT molecules on a sufficiently extended Cu(111) slab at >10 different relative orientations and separations, including various ones that allow for interaction via H_{ortho}, H_{meta} and H_{para}. For each of the three interactions, the background of Fig. 3.2c shows the configuration associated with the most pronounced lowering of the total free energy by 102 meV, 88 meV & 42 meV compared to separated molecules, respectively. These results show a wide distribution of S···H-C bond length of 3.6 Å, 3.9 Å & 3.1 Å, respectively. The sequence of interaction energies corroborates our experimental observation of the dominance of the H_{ortho}-atom

in intermolecular interaction and it is in good agreement with previous work on fluorinated species.[53, 66]

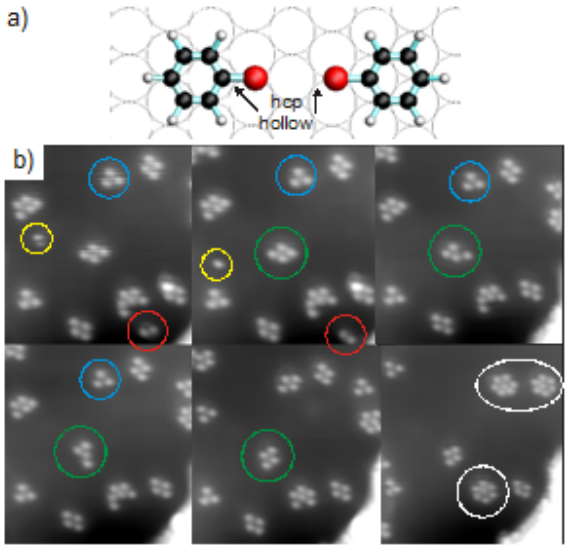

Figure 3.1 a) BT and its adpositions on Cu(111) from Ref. [64]; b) sequence of STM images (-1.4V, 34pA) during the annealing of BT/Cu(111) from 50K to 90K. Initially individual molecules (yellow) become mobile followed by dimers (red). Trimers (blue) are very stable and often attach another molecule (green) on the periphery, which can rearrange itself facilely. Ultimately, the majority of molecules form stable heptamers.

Upon further anneal of the molecular population of Fig. 3.1, triangular trimers – most commonly of the kind shown in the background of Fig. 3.2c - are found (blue circle), yet also other trimers (see Fig. 3.2a,b) exist. Fig. 3.2c compares the abundance of triangular trimers to that of trimers of all other shapes (i.e. not only the linear one shown). It should be noted that trimers composed of a closed loop of both H_{ortho}- and H_{meta}-interacting molecules are sterically possible, yet the latter are rarely observed. During our measurements, trimers frequently attach another molecule that subsequently changes

position and configurations quite rapidly (green circle), leading us to interpret most tetramers as a stable trimer with an additional molecule attached. No tetramers with a 'circular' interaction pattern (like for the pictured trimer) have been observed. Ultimately, virtually the entire population of BT is converted into heptamers that incorporate both H_{ortho}- and H_{meta}- interactions. Similar to the trimers, these heptamers shield their sulfur atoms from interacting with additional molecules. Consequently, they do not form the nucleus for larger ordered aggregates, and no ordered surface coverage emerges.

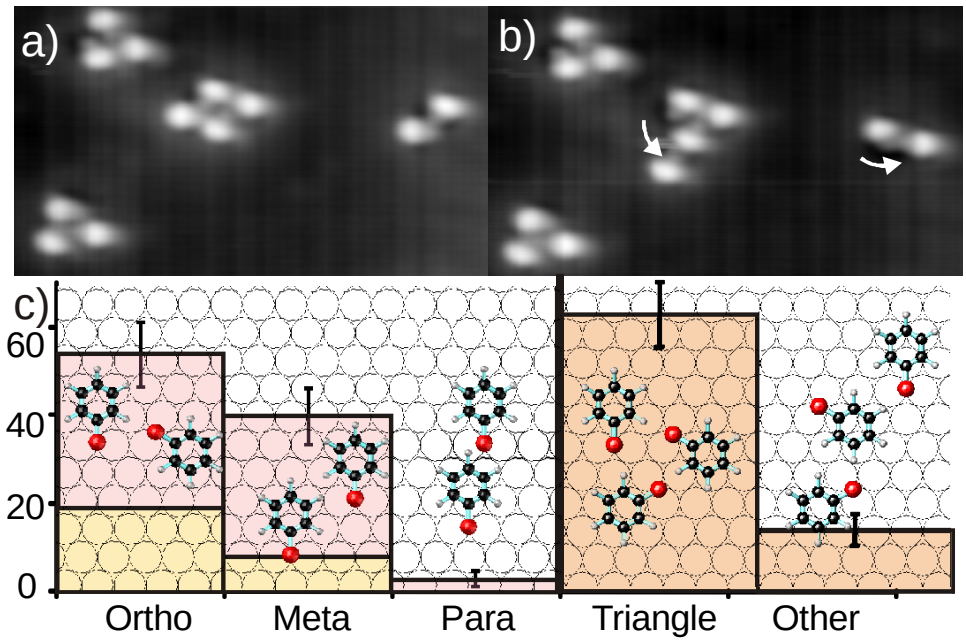

Figure 3.2 a,b) STM images resolving the benzene ring (bright) and sulfur anchor (gray shoulder) of BT. Two triangular trimers and rearrangement of a tetramer and an H_{ortho}-interacting dimer are visible. 2c) Statistical evaluation of dimers show that the majority of them interacts via H_{ortho} followed by H_{meta}. Trimers tend to form triangles (as in panels a,b) rather than any other pattern (not only the one shown).

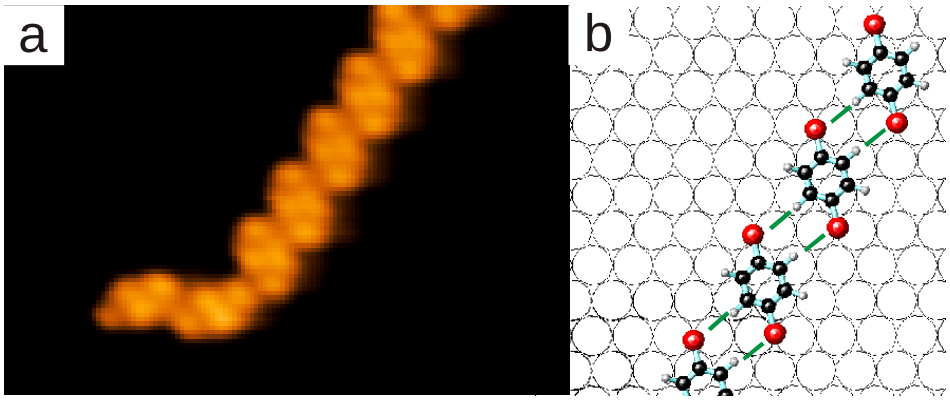

Figure 3.3 a) Row of BDT molecules interacting via Hortho (-2.0V, 31 pA) and corresponding model (b).

The evolution of the BT coverages is reminiscent of Oswald ripening, a common feature in e.g. metal epitaxy, which has also been observed for molecules.[67] Due to the anisotropic nature[68] of the BT-BT interaction epitomized by the dominance of H_{ortho} in intermolecular interactions (in contrast to the isotropic interactions of e.g. metal atoms), the formation of stable 'magic' clusters at relatively small cluster size was observed. [69] Is the dominance of one particular hydrogen atom a general feature of intermolecular interaction in arenethiol films? To address this question, coworkers and I proceed in two directions: (i) conversion of all BT hydrogen atoms to H_{ortho} by addition of a second thiol group (resulting in BDT) and (ii) extension of the arene moiety to anthracene.

STM images of a low coverage of BDT show the formation of chains (Fig. 3.3), in which each sulfur interacts with an H_{ortho}-atom of a neighboring molecule. BDT adsorbs with both sulfur atoms near bridge sites, which positions the arene ring at an

asymmetric configuration with regards to the substrate (in contrast to BT, Fig. 3.1a), thereby allowing H_{ortho}-interactions between parallelly adsorbed molecules. The importance of H_{ortho} interactions is further underlined by the fact, that upon increase of the BDT coverage a variety of patters emerge that are characterized by interwoven rows similar to the H_{ortho}–rows shown in Fig. 3.3a.

3.3.2 Anthracene Deravatives

Can a similar prevalence of one particular hydrogen atom in intermolecular interaction of a different arene backbone be found? To strengthen the notion that arenethiol pattern formation is determined by the optimization of the intramolecular interaction of the hydrogen atom in one particular position on the ring, anthracenethiols were explored.

AT (the anthracene counterpart of BT) forms a surface pattern with an almost square $\begin{bmatrix} 3 & 3 \\ 1 & -4 \end{bmatrix}$ lattice (Fig.3.4 a,c): each molecule adsorbs at a position and orientation similar to BT while aligning the anthracene moieties in parallel rows, with successive rows offset by 2.5 lattice vectors along the row direction (Fig. 3.4d). This places the sulfur atom of one molecule in close proximity to the hydrogen atoms in 3&6 positions of the two molecules in the adjacent row. Based on this observation, coworkers and I explore whether the hydrogen in position 3, or more generally the terminal hydrogen atom of the anthracene system, are the ones that dominate the intermolecular interaction (and thus determine the film pattern) for anthracenethiols on Cu(111).

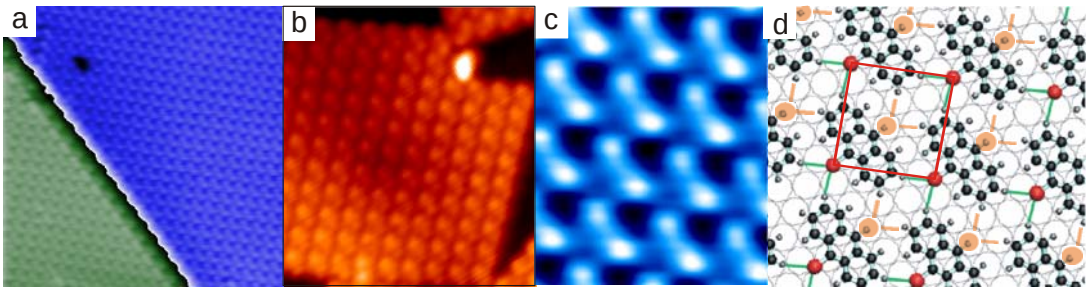

Figure 3.4 a,b) STM images (-0.9V, 94pA and -2.3V, 79pA) of AT and ADT on Cu(111), respectively, showing successive molecular rows in antiphase (zoomed in at panel c). d) molecular model of the pattern with unit cell and intermolecular bonds for AT (green) and ADT (orange) indicated.

Addition of a second thiol group to AT at the opposite side of the ring results in ADT, which forms the same $\begin{bmatrix} 3 & 3 \\ 1 & -4 \end{bmatrix}$ lattice as AT (Fig. 3.4b). Due to the presence of sulfur atoms on both sides of ADT, all terminal hydrogen atoms are equivalent (save for a difference in adsite of the sulfur atoms),[25] and they are all involved in intermolecular interactions (Fig. 3.4d), yet the inequivalent hydrogen atoms in positions 1,4,5,8 do not participate.

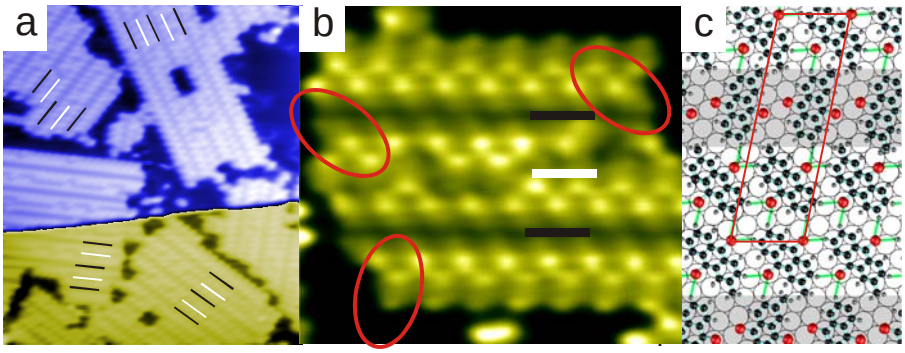

Figure 3.5 (a and b) MADT islands (-1.5V, 85pA/-2.2V, 49pA) showing double rows of molecules that present their protruding methyl groups to the outside. The inside of these rows appears as a depression running along the row direction. It is highlighted with a black bar in panels a,b and corresponds to the unshaded area of panel c. These double rows are separated by a single row of molecules at a different yet equivalent surface orientation presenting their methyl groups to either side randomly causing a disordered appearance of this row (highlighted with a white bar, shaded region in panel c). The orientation of the molecules is visible at the row edges indicated with ellipses.

Fig. 3.5a,b) MADT islands (-1.5V, 85pA/-2.2V, 49pA) showing double rows of molecules that present their protruding methyl groups to the outside. The inside of these rows appears as a depression running along the row direction. It is highlighted with a black bar in panels a,b and corresponds to the unshaded area of panel c. These double rows are separated by a single row of molecules at a different yet equivalent surface orientation presenting their methyl groups to either side randomly causing a disordered appearance of this row (highlighted with a white bar, shaded region in panel c). The orientation of the molecules is visible at the row edges indicated with ellipses.

Coworkers and I further explore which impact introduction of steric hindrance (by means of methyl groups) has on the film pattern. In particular, we wish to elucidate, whether the dominance of the original H_{term}-based intermolecular interaction persist forcing the film to adopt a more complicated geometry to accommodate both the interaction and the steric hindrance at the same time, or whether the steric hindrance suppresses the original kind of interaction permitting another kind of intermolecular interaction to shape the film pattern.

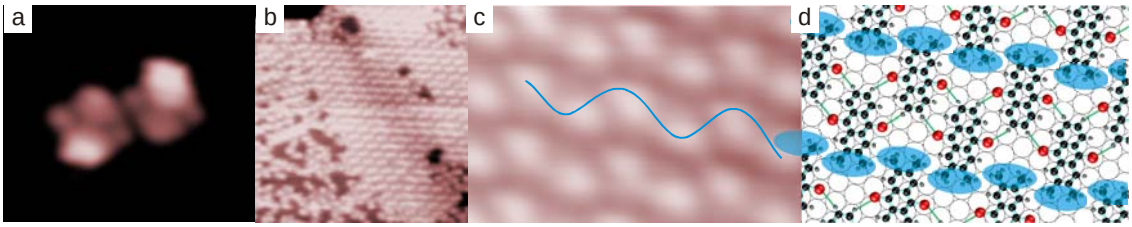

Figure 3.6 a,b,c) Individual DMADT molecules and film pattern (-0.4V, 45 pA / -1.0V, 78 pA /-0.4V, 45 pA) consisting of parallel molecular rows with alternating orientation of the methyl groups leading to a wavy pattern (blue lines) of protrusions representing the methyl groups (panel d).

Replacement of one of the terminal hydrogen atoms with methyl results in MADT. Due to its lower symmetry, an MADT film (Fig. 3.5a,b) adopts a more complex pattern characterized by alternating rows of linear depressions that appears to be flanked by ordered rows of protrusions (highlighted black in Fig. 3.5a) and disordered zig-zagging depressions (highlighted white in Fig. 3.5a). At higher magnification (Fig. 3.5b) it becomes apparent that the first kind of linear depression reflects a double row of molecules pointing their protruding methyl groups to the outside. This allows their anthracene and thiol moieties to interact in the inside of the row as if not substitution were present (unshaded portion of Fig. 3.5c). Due to the lack of methyl-induced protrusion, this portion of the film appears as an indentation. These double rows of molecules are separated from one another by a row of molecules whose anthracene moiety is rotated by 120 degrees with regards to those in the double rows (resulting in an equivalent adsite due to the 3fold symmetry of the Cu(111) substrate). These molecules interact with one another in the same way as those in the double rows and they point their

extra methyl group at random either towards the one or the other of the adjacent double rows giving rise to the disordered appearance of this row. In combination, there are three molecules per unit cell, which can be represented in matrix notation as $\begin{bmatrix} 11 & 3 \\ 1 & -4 \end{bmatrix}$. The H_{term}-interactions in this film are highlighted in panel c of Fig. 3.5; counting their number it becomes apparent that they are the dominant way of intermolecular interaction despite the low symmetry of the individual molecules.

Methyl-substitution of all terminal hydrogen atoms on one side of ADT leads to DMADT, which forms a pattern (Fig. 3.6a-c) reminiscent of A(D)T: the molecules align their anthracene moieties in rows with successive rows pointing the methyl groups in opposite direction. Along the anthracene rows, the molecules are separate by one more substrate lattice spacing to accommodate the extra methyl groups. Adjacent rows arrange the methyl groups to opposite sides, so that the methyl groups form a line meandering perpendicular to the row direction through the film (blue line), rendering the impression that an indentation (the unsubstituted side of the molecules) meanders in parallel. Counting the S…$H_{terminal}$ interactions indicated green in panel 6d, it becomes apparent that this film also favors this particular kind of intermolecular interactions.

Thus, films of four different anthracenethiol species were found adopting patterns tailored to optimize the intermolecular interactions of the hydrogen atom at the terminal position of the acene. Does this only occur in extended films, or is this interaction also

dominant for small aggregates of molecules (like the H_{ortho}-based interaction in BT aggregates)? To answer this question, coworkers and I also imaged low coverages of these molecules. Previous studies already showed row formation for ADT,[25, 26] at a periodicity identical to the ADT film pattern, i.e. in these rows both sulfur atoms of one molecule interact with the $H_{terminal}$ atoms of their neighbors. MADT (Fig. 3.7b) and DMADT (Fig 3.7c) form the same kind of row, with the extra methyl groups avoiding perturbation of the S···$H_{terminal}$ interaction by pointing to either side of the row at random (MADT) or alternatingly (DMADT) again highlighting the particular role of the terminal position for intermolecular interaction.

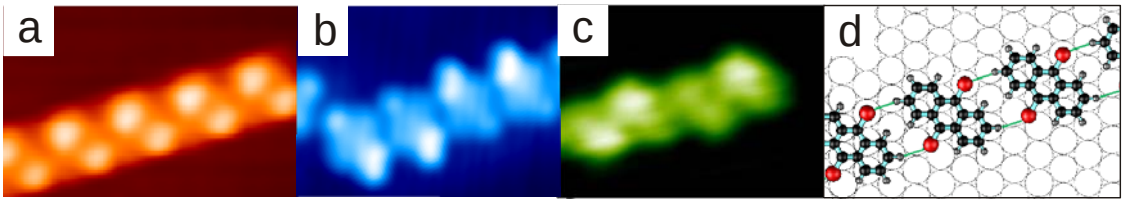

Figure 3.7 STM images of rows of (a) ADT, (b) MADT, (c) DMADT (-1.5V, 79pA; -1.5V, 85pA; -3.0V, 41pA) and (d) model showing the molecular setup and hydrogen bonding in this configuration. The methylated species adopt the same pattern.

3.4 Discussions

The investigation of two and four members of two classes of arenethiols on Cu(111) reveals that for each class film patterns emerge that optimize the S···H intermolecular interaction in one particular position on the aromatic system. This suggests that once this position is identified for one particular molecular backbone and substrate, the film

patterns of differently substituted molecules can be predicted. At this point it remains to be answered, what is special about these particular hydrogen atom positions.

Geometrically, H_{ortho} has the longest C-H bond in the molecule both in the gas phase and on the surface, suggesting that it is most prone to intermolecular interaction. Also in terms of Lewis acid/base complexes, H_{para} lies at a node of the LUMO of BT. As such, HOMO-LUMO interactions should prefer $H_{ortho/meta}$. Indeed, a preference for H_{ortho} has been reported earlier for fluorine containing compounds.[53, 66] The case is less straightforward for anthracene derivates, where the $H_{terminal}$-bond is longer in calculations for the gas-phase, but indistinct bond lengths are found in surface calculations.

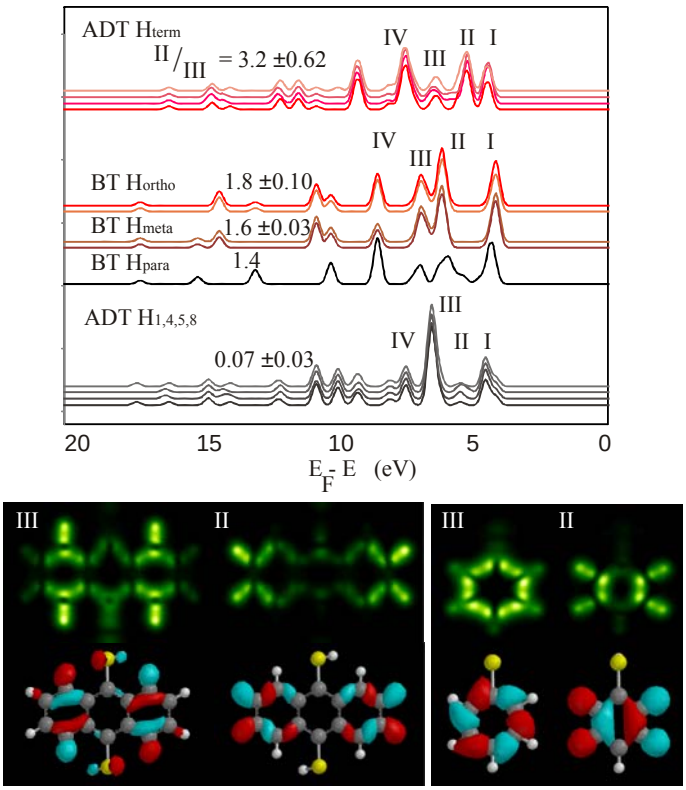

Figure 3.8 (top) Calculated density of states at the location of the hydrogen atoms. The ratio of the weight of states II and III (indicated error based on variation between atoms equivalent in the gas phase) correlates with the propensity of the atom in intermolecular interaction. (bottom) Charge density of states III and II for the adsorbed molecule (using energy intervals of 6.75-6.35 eV, 5.43-5.03 eV, 7.02-6.75 eV and 6.22-5.96 eV below EF, respectively) and the corresponding gas-phase molecular orbitals (found at 6.6 eV, 5.1 eV, 5.9 eV, 5.0 eV below HOMO).

Our DFT calculations of the surface-bound molecules find charge density at the hydrogen atoms of the molecules as shown in the top of fig. 3.8. The spectra show only occupied states, i.e. states below the Fermi level. Due to the node of the π system in the plane of the hydrogen atoms, no π-derived states are evident (including the HOMO). The highest energy feature with significant density at the hydrogen atom (marked I in fig. 3.8)

derives from the d-bands of the substrate, followed by several states stemming from the σ-system of the aromatic moiety. Notably, the second (II) feature appears to correlated with the propensity of an atom for taking part in intermolecular interaction, whereas the third (III) feature, in particular for ADT, is dominant, if no hydrogen bonding occurs based on the corresponding atom: for ADT, where interaction exclusively via H_{term} and not via the internal hydrogen atoms was found, the ratio between the weights of feature II and III are 3.2 vs. 0.07, respectively. For BT, where a more gradual preference for H_{ortho} over H_{meta} over H_{para} was found, the ratios are 1.8 vs. 1.6 vs. 1.4. Why do these states affect the propensity of the hydrogen atoms for intermolecular interaction?

The bottom panel of fig. 3.8 shows a projection of their extent. For comparison, the figure also shows the corresponding states as calculated for the gas phase, where the nodal structure can be calculated directly. The projections show that feature II corresponds to a orbital pointing to the periphery of the molecule both for BT and ADT. In contrast, feature III places more weight inside the molecule. As the availability of charge density at the periphery of a molecule is crucial for hydrogen-bond-based intermolecular interaction with its neighbors, these findings provide a quantum level rational for the experimentally observed dominance of the intermolecular interaction of one particular hydrogen atom in each system. The prominent positions of these states in the electronic spectra suggest that the hydrogen atom position dominating intermolecular

interaction may be derived straight-forward from theory rather than requiring any measurements at all.

3.5 Conclusion

Coworkers and I addressed several members of two families of arenethiols systematically and found that their film patterns are tailored to optimize the intermolecular interactions of the hydrogen atoms in particular positions on the arene – and that this predominance of one positions persists upon further inert or thiol substitution of the arene. In combination, our findings suggest that once for a class of arenes the dominant H-atom position is identified, the patterns of inertly substituted species can be predicted, at least on Cu(111). Moreover, the dominant position on the arene can be rationalized straightforwardly from DFT calculations of the adsorption configuration and it is in good agreement with conventional chemical behavior of the molecule, suggesting an even further degree of predictability of the molecular film patterns.

Chapter 4

Tunability in polyatomic molecules

(From publication: Journal of American Chemical Society, 2010, 132, 13578–13581)

4.1 Introduction

The development of molecular machines as realization of the ultimate miniaturization of macroscopic devices has become a research topic of general and widespread interest. Molecular machines are common in the biochemical arena (F1-motor of ATP synthase, proton pump in cell membranes, transcription polymerase, kinesin motor proteins, etc.). Much smaller and easier to handle molecules have been synthesized to resemble macroscopic devices such as gears,[70] cars,[71] ratchets,[72] walkers,[24, 25, 73] turnstiles,[74, 75] pinwheels,[76] shuttles,[77] 'sky-hooks'[78] and wheel-barrows[79] when adsorbed at a metal surface.[80-83] For surface molecular machinery to obtain ultimate utility, it is necessary that their motion is reliable and their rate of motion tunable in a predetermined fashion to the task at hand. Here coworkers and I report on a class of molecules that allows us the study of the transition from tunneling diffusion to conventional over-barriered diffusion and permit tuning of the diffusion temperature between 20 and 80 K.

4.2 Experimental

All measurements in this study were performed in a scanning tunneling microscopy (STM) instrument capable of imaging molecular diffusion at 8K and above in ultra-high vacuum. Preparation of the Cu(111) sample involved sequences of sputtering and annealing, followed by cooling to 80K. Deposition of the molecules from a glass capillary proceeded on the cryogenic sample followed by annealing to close to room temperatures to desorb inevitable solvent residues. Temperatures were measured by a silicon diode attached to the STM scanner, which in turn had been calibrated by replacing the STM tip with a silicon diode in the tip-holder-sample junction. In combination, this results in a temperature uncertainty of +/- 1K.

All density functional theory simulations utilized the VASP code[60] with the generalized-gradient approximation[6] for the exchange-correlation functional and the plane-wave pseudopotential method[61] with ultrasoft pseudopotentials.[21] Our calculations use a 4x8 substrate atoms supercell with 4 substrate layers that provides sufficiently large lateral extent to prevent intermolecular interactions despite circular boundary conditions. The atom positions were optimized so that all forces in the system are smaller than 0.04 eV/Å.

4.3 Results

In previous work anthraquinone[24] (AQ) (and its sulfur counterpart dithioanthracene[25], DTA) has been shown to diffuse on sixfold symmetric Cu(111) exclusively along the high-symmetry direction indicated by its aromatic moiety, i.e. violating the substrate symmetry, which is accomplished by sequential placement of its chalcogen substrate linkers, a process dubbed ‘walking’. While AQ movement proved useful in carrying cargo, its very low apparent diffusion prefactor of just $10^{2.4}$ Hz and barrier of 0.02 eV indicates a diffusion mode that is not well understood. Here it is shown that modification of AQ can lead either to similar or to much higher diffusion barriers and prefactors, depending on whether the resultant molecule can adopt a diffusion mode, in which tunneling of a single atom across a barrier can forward it.

Coworkers and I investigated the surface diffusion of pentaquinone (PQ), pentacenetetrone (PT) and a derivative of PT carrying methyl groups at diagonally opposed ends of the aromatic backbone (DPT). The first two species were obtained commercially, and DPT was synthesized through dimerization of suitably substituted naphtaquions. While PQ differs from AQ only by extension of the ring system and thus may be expected to diffuse in a similar way across a surface, PT and DPT have four substrate linkers and potential docking sites for molecular cargo, inviting the question, in which fashion a quadrupedal species moves on a surface. Will it be in a walking style at all? And if it is a walking style, which gait will its legs adopt: trotting, in which

diagonally opposed legs move in unison, or pacing, in which the legs on one side of the molecule move alternating with those on the other side?

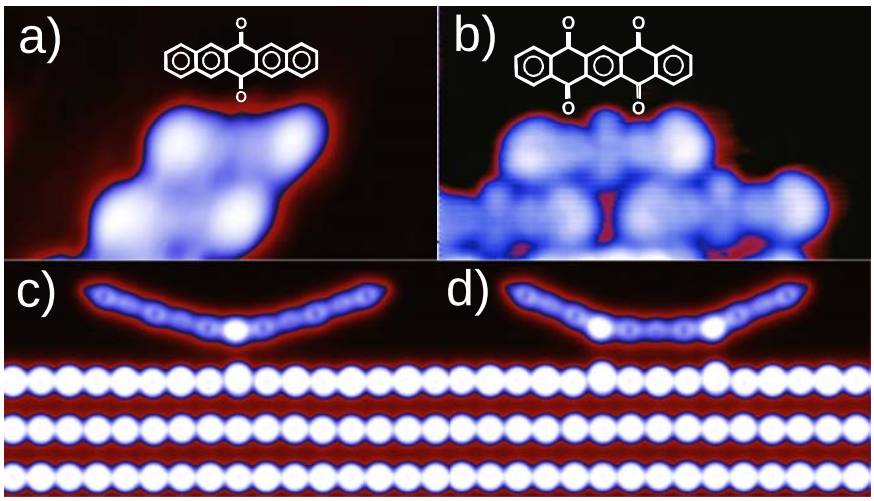

Figure 4.1 (a,b) STM images of PQ (a) and PT (b) on Cu(111). (c,d) Integrated charge density from density functional theory simulation of PQ (c) and PT (d) on Cu(111). PQ is pinned by its sets of carbonyl linkers to the substrate allowing its peripheral portions to bend away from the latter, whereas PT is pinned down by its two sets of carbonyl linkers only allowing its terminal aromatic rings to levitate. STM image parameters: (a) 93 pA, -1.7 V, 37Å × 22Å; (b) 130 pA, -1.1 V, 32 Å × 19 Å. Due to the antiphase nature of successive (110) atomic rows on Cu(111), the substrate atoms appear twice as closely spaced.

Coworkers and I found that PQ adsorbs on Cu(111) very similar to AQ,[24] i.e. with its anthracene body aligned with one of the substrate atomic rows (Fig. 4.1a). It appears as an elongated protrusion in STM images with slightly narrower waist at the carbonyl group position. DFT simulation of it adsorption configuration shows its carbonyl substrate linkers pinned to the substrate with the remainder of the molecule bending upward (Fig. 4.1c), similar to AQ. Fig. 4.1b and d show an STM image of several PT molecule on a Cu(111) surface and a cross section of the adsorption configuration

obtained by integrating the charge density across planes normal to the surface and the molecule. The molecular axis is aligned with one of the atomic rows of the substrate. Its four carbonyl oxygen legs come to rest on the surface, pulling the second and fourth aromatic ring down onto the substrate, while allowing the terminal rings to lift upwards. DPT adsorbs similar to PT on Cu(111).

Sequences of STM measurements reveal that PQ, PT and DPT diffuse exclusively along the axis indicated by their aromatic moiety, similar to AQ.[24] Several days of diffusion data on each of the molecules were acquired and in several thousand diffusion events investigated, no perpendicular motion or rotation has been observed.

Plotting the molecular diffusion rate versus the experimental temperature leads to the Arrhenius plot of Fig. 4.2, which in addition to the PQ, PT and DPT also shows the diffusion rate of AQ for reference.[24] The statistical error is smaller than the data markers. From these data diffusion barriers of 0.02 eV +/-0.01 eV and 0.03 eV +/-0.01 eV for AQ and PQ, respectively, and of 0.13 eV +/-0.02 eV and 0.19 eV +/-0.02 eV for PT and DPT, respectively, can be extracted. Although the largest variation in diffusion barrier is found between bipedal and quadrupedal species, the difference in diffusion barrier induced by methyls substitution and elongation of the ring system is substantial (i.e. ≈ 50% each). For example, extrapolation of the diffusion rate of the methylated species to the unmethylated one indicates almost a millionfold difference in diffusion rate.

The effect of methylation is even sufficient to put the observation of uniaxial diffusion within reach of LN_2 cooling. These results make it clear that terminal methyl substitution and backbone elongation, despite their chemically inert nature and remote location from the fulcrum of the motion, are very sensitive handles for tuning of the diffusion rates of walking molecules.

The difference between bipedal and quadrupedal species is even more striking, if the prefactors are compared. For AQ and PQ diffusion the prefactors are $10^{2.4+/-1}$ and $10^{2.3+/-1}$, respectively, whereas the prefactors for PT and DPT are both $10^{13+/-1}$ Hz. The prefactors for the bipedal species are much lower than the conventional 10^{10}-10^{13} Hz, yet low prefactors have been reported in a number of STM diffusion experiments at low temperatures: CO/Cu(111): $\approx 10^7$ Hz;[84] CO chevrons/Cu(111): $\approx 10^5$ Hz;[85] CO/Cu(110): $\approx 10^7$ Hz[86]; Al/Au(111): $\approx 10^3$ Hz[87]). A concerted lowering of prefactors and barrier has been described already 70 years ago, named the Meyer Neldel or compensation effect,[88, 89] and has since been observed for a range of phenomena including conductivity of organic semiconductor, mobility of polymers, grain and phase-boundary motion, etc. [90] Yet the magnitude of reduction observed here is larger than expected, raising the question for what sets quadrupedal motion apart from bipedal.

To this end, coworkers and I performed DFT simulation how PT overcomes the diffusion barrier. Starting out from the initial minimized configuration we move the

substrate linkers successively by 0.1-0.2 Å at a time followed by minimization of the entire system so that all forces are smaller than 0.04 eV/Å keeping only the forward motion of the manipulated oxygen atoms fixed. In previous mapping of the diffusion potential for AQ and DTA we showed that the molecule moves by alternating stepping its substrate linkers, angling the molecule with regards to the substrate.[24, 25] For the quadrupedal species mapping of the entire parameter space is computational prohibitive, because it is not two dimensional as for AQ but four dimensional. Rather we investigate the diffusion barrier along three potential pathways: a pathway, in which two diagonally opposed ones substrate linkers move at a time resembling the gait of trotting (Fig. 4.3b); one, in which two adjacent substrate linkers move at a time resembling pacing (Fig. 4.3c); and one, in which the molecule glides across the surface (Fig. 4.3d). Using the mean forward motion of the substrate linkers as reaction coordinate, the diffusion barriers of Fig. 4.3e result.

Each of the diffusion pathways is associated with more than one barrier. During trotting, the diagonally opposed substrate linkers move and the remainder stay stationary causing the molecule to distort. The maximum distortion is reached at ¼ (and ¾) of the step distance coinciding with the maximum barrier of (0.7-0.8 eV). At the diffusion midpoint, the distortion of the molecule is released leading to a relatively low energy state, despite the fact that in this configuration the interaction with the substrate is not optimal. In the second half of the trotting motion the other set of diagonally opposed

atoms leads. The diffusion barrier encountered during trotting is significantly higher than the measured value and prohibitive at the temperatures of our experiments. It reflects the great energetic cost in distorting the molecule due to the stiffness of its aromatic backbone.

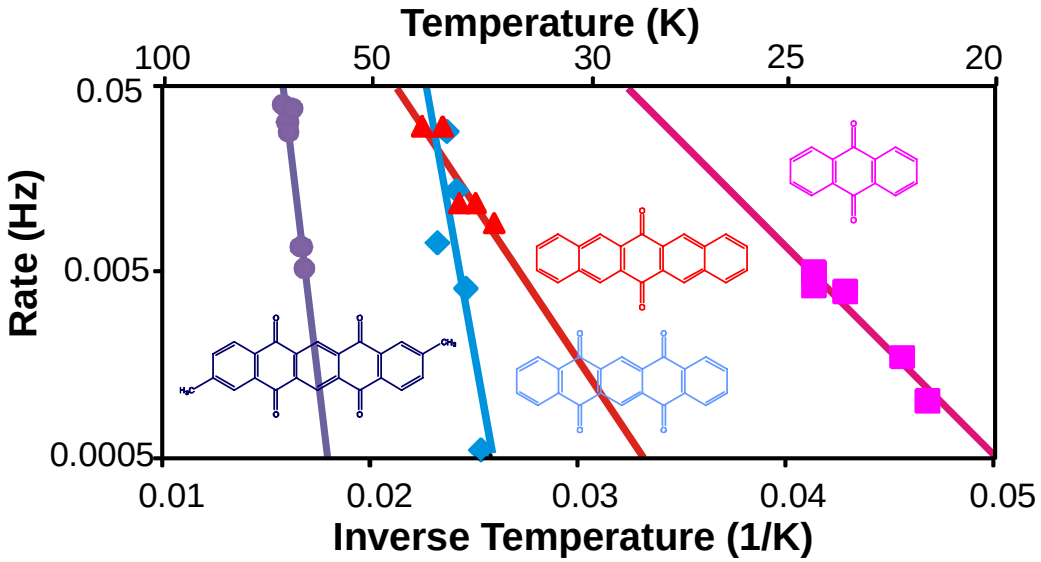

Figure 4.2 Arrhenius plot of the uniaxial motion of AQ (pink), PQ (red), PT (blue) and DPT (purple).

On the gliding pathway (and to a lesser degree on the pacing pathway), initial displacement from the equilibrium adsite comes at a (small) barrier. While pacing, the second set of substrate linkers starts moving once the first set reaches 1/4 of the diffusion distance merging the molecular setups for pacing and gliding at the diffusion quarterpoint (≈ 0.6Å) at an energetic minimum. Similarly, all diffusion pathways merge at the diffusion halfpoint and the molecule is aligned parallel to the diffusion direction. In

gliding, PT approaches this point via a considerable barrier, whereas in pacing, the molecule angles itself barrierless into this configuration, rendering pacing motion energetically more favorable. Pacing and gliding motion are inversion symmetric with regards to the first and second half of the diffusion step.

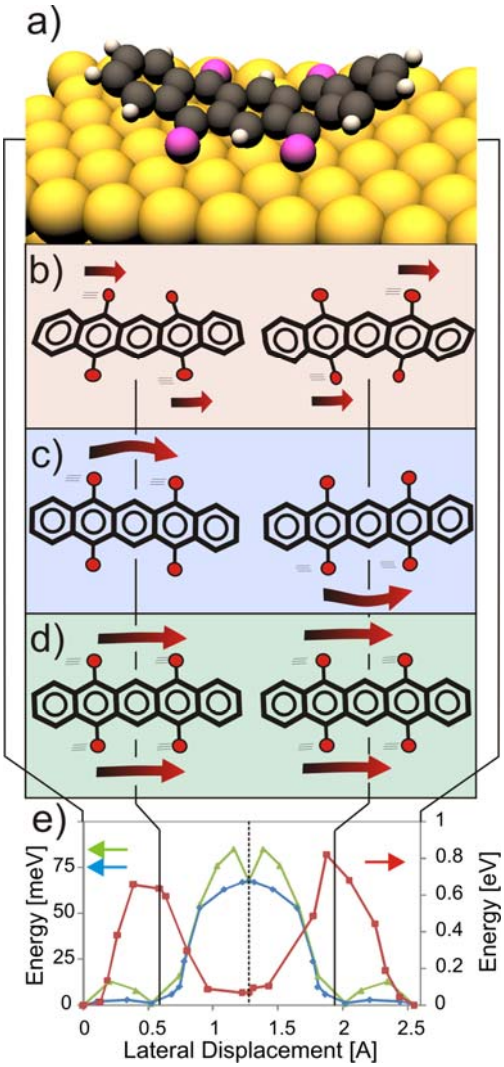

Figure 4.3 Setup of PT on Cu(111) as obtained from DFT-based minimization (a) and schematic representation of trotting (red), pacing (blue) and gliding (green). Panel (e)

shows the corresponding energy barriers, with trotting on the right y-axis and pacing as well as gliding on the left axis.

The absolute height of the simulated diffusion barrier of ≈ 0.07 eV is somewhat lower than the experimental value of 0.13 eV; van de Waals (vdW) interactions are absent from our DFT simulations for reason of computational feasibility. These contribute substantially to the acene-substrate interaction explaining the difference in total barrier.[91, 92] While this may also impact our assignment of the gait, it is believed that the 0.02 eV difference in energy between pacing and gliding will not be superseded by vdW interactions given their typically slow spatial variation.

The simulation results indicate that the motion of the molecular backbone during diffusion is quite similar for bipedal and quadrupedal species, yet in the quadrupedal motion the substrate linkers need to occupy inequivalent adsites. In the pacing gait two substrate linkers necessarily move at the same time; in contrast to the energetically prohibitive trotting, where sequential movement of the substrate linkers is conceivable. What implication does this have for understanding the variation in diffusion prefactors between bipedal and quadrupedal species?

Tunneling has been discussed as a mechanism for low-temperature diffusion of hydrogen atoms and also for CO diffusion on Cu(111) by Eigler's group,[85, 93, 94] who found indications that the mass m relevant for tunneling is exclusively that of the

substrate-attached atom (i.e. carbon in the case of CO molecules) and not the entire molecule. Thus, in the case of the molecules investigated here, the tunneling species may just be the oxygen (carbonyl) substrate linker. Tunneling can require thermal activation, i.e. once the molecule has thermally reached a certain vibrationally exited state the remaining barrier height E_{atom} and depth d is crossed via tunneling.[85] Then an Arrhenius analysis will still result in a straight line but the barrier height E_{barr} obtained corresponds to the energy of the required vibrational activation. The apparent attempt frequency is the product of the attempt frequency leading to occupation of the vibrationally excited state and the tunneling probability P from that state across the barrier.[95] P can be estimated in the Wentzel-Kramers-Brillouin (WKB) method[85]:

$$P = e^{-2/\hbar \int_0^d \sqrt{2mE_{atom}(x)}\, dx}$$

Assuming the central portion of the pacing barrier (Fig. 4.3e) as $E_{atom}(x) + E_{barr}$, a tunneling probability of ≈ 10-10 results. Thus, if the rate at which the bipedal AQ species approaches the vibrationally excited state is assumed to be a typical value of $10^{12} – 10^{13}$ Hz, an apparent attempt frequency of $10^2 – 10^3$ Hz is expected, which corresponds to the values measured here.

Why then were low prefactors for the bipedal species and conventional ones for the quadrupedal one observed? The simulation showed that molecular distortion required to place the substrate linkers sequentially (as it is possible in the trotting gait), is

energetically prohibitive. Pacing, however, requires concerted motion of both substrate linkers on one side of the molecule; yet concerted tunneling of them has a probability of $P^2 \approx 10^{-20}$, too unlikely to occur. Thus, tunneling is only an option for a molecule, in whose motion no concerted displacement of substrate linkers is required.

4.4 Conclusion

The combination of modeling of the diffusion mode and the calculation of the tunneling probability provide a strong argument in favor of the relevance of tunneling for the bipedal species. Moreover, the apparent barriers obtained from the Arrhenius fit of AQ and PQ diffusion of 0.02 eV and 0.03 eV are a much better match for vibrational modes of oxygen atoms at surfaces, as required for thermally assisted tunneling, than for actual diffusion barriers.[96]

Chapter 5

CO adsorbates within nano scale pores on Cu(111)-Part1

(From publication: Nano Letters, 2010, 10,3700–3703)

5.1 Introduction

Nanoscopic metal facets have considerable technological relevance, for instance on supported metal catalysts for applications ranging from the (petro-)chemical industry to emission control, yet the diffusive behavior of adsorbates has so far generally been studied on extended terraces, i.e. not under lateral confinement, mainly due to experimental obstacles. For the study of the dynamics of adsorbates on nanoscale clusters, it would be ideal if arrays of atomically identical ones could be formed. Absent this possibility a Cu(111) substrate covered with a self-assembled anthraquinone network was utilized. This network sustains subsequent deposition of CO molecules and confines their diffusion into pores of ≈ 4nm in size, where they can be imaged and studied in detail.

The pores have a similar size as the facets expected on catalytic nanoclusters; in particular, studies on gold have shown that its activity increases enormously if dispersed in this size regime.[97, 98] Conventionally, the high activity of nanoparticles, as compared to the surfaces of bulk metals, is attributed partly to the high surface to volume

ratio at high dispersion, and partly to support-metal interactions and the abundance of surface defect sites such as step-/facet-edges and -kinks.[99] While the exposed copper facets of our network probably have little besides their size in common with catalytic nanoparticles, they nevertheless open for study the kind of effects that lateral confinement may have on the dynamics of adsorbates, at least in a phenomenological manner; a survey of them is the objective of this study.

Several previous publications addressed the dynamics of adsorbates at metal surfaces and their interaction with one another. They include measurements of the dynamics of benzene molecules,[100, 101] reactive mixtures,[102, 103] hydrogen atoms,[104] and CO molecules.[84-86, 105-107] Also, the insertion of atoms or molecules into molecular surface networks has been studied previously.[41, 108-112] What makes our study novel is the confined nature of the adsorbates that allows us to study how molecules behave when their support is not a large, clean and inert terrace.[113]

5.2 Experimental

CO was used as a test molecule because abundant data on its surface behavior is available: CO molecules adsorb upright atop Cu(111) substrate atoms. They are imaged in scanning tunneling microscopy (STM) as protrusions or indentations, depending on whether the STM tip is decorated with a CO atom at its apex or not, respectively.[114] At

sufficient coverage, CO adsorbates form an ordered (√3x√3)R30° overlayer; large islands of this superstructure have been observed in previous STM studies.[115] In our model system there are 186 exposed atop adsites in each 4 nm pore, allowing a maximum occupation in the exposed facet of 62 CO molecules in a dense (√3x√3)R30° adlayer.

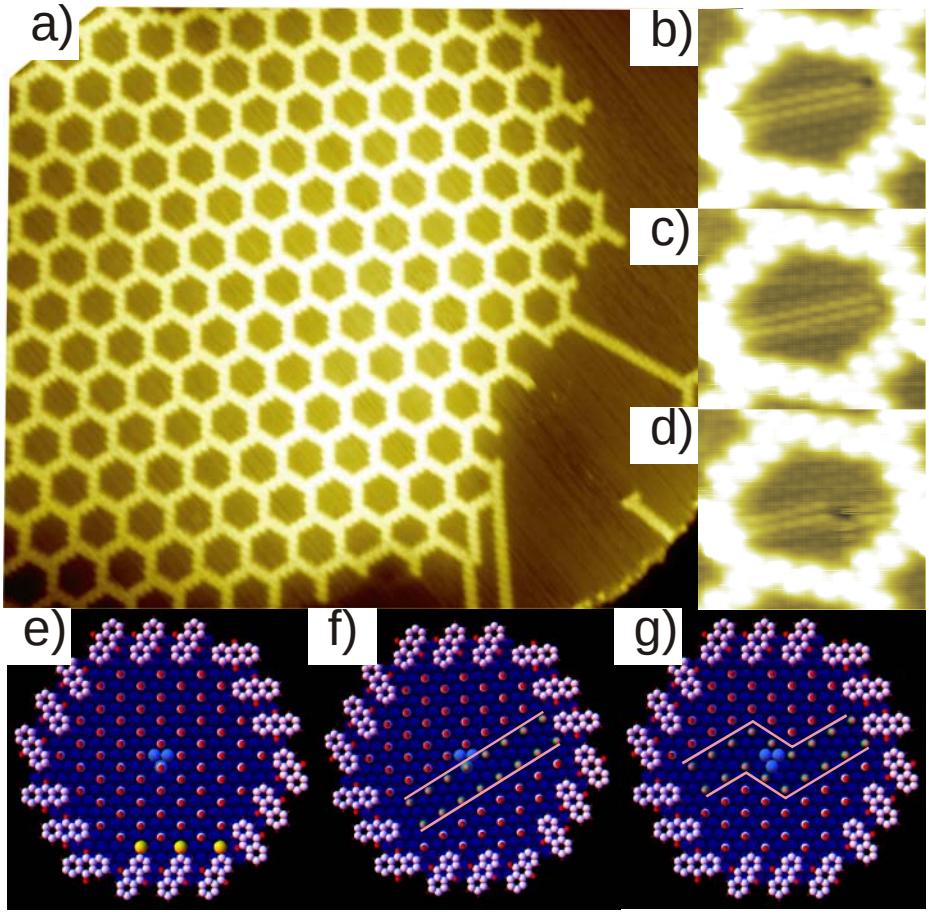

Figure 5.1 a) array of atomically defined pores on Cu(111) formed by deposition of anthraquinone according to Ref. [27] Image parameters: 83 nm x73 nm; Bias: -2.53V; Current: 50 pA, Temperature 90 K; b,c,d) images from a STM movie of a dislocation line moving in confinement. Image parameters: Bias -2.40 V, Current 44 pA, Temperature: 24 K e,f) The (√3x√3)R30° adlayer can be anchored at any one of the three atoms at the center of the exposed facet (light blue). In each case, one facet edge is decorated differently than the remaining two of the same kind (yellow in e). This can be alleviated, if a dislocation line is induced in the pore (f). In both cases the same number of molecules

fit inside the pore. g) Model of a kink in a dislocation line similar to the STM image of panel d.

Initial sample preparation involves the usual sequence of sputtering and annealing, followed by cooling to liquid nitrogen temperatures. The anthraquinone pattern is created by deposition of the molecule onto the cryogenic sample followed by annealing to room temperature. After subsequent cooling to ≈ 40 K , CO is deposited through a leak valve.

5.3 Results

Deposition of CO molecules into an anthraquinone honeycomb network does not alter the pore shape. With careful dosage a CO coverage very close to a complete (√3x√3)R30° overlayer was obtained, which is visible inside the pores (Fig. 5.1b-d). Moreover, on the exposed facets a dislocation line was found, which is constantly present yet persistently shifting position. This differs from the behavior of CO films on extended terraces, where the (√3x√3)R30° is observed over large areas and dislocation lines (i.e. antiphase domain boundaries) are expelled to the edge.[115] What is the origin of this effect?

Each exposed facet is centered around a substrate hollow site, allowing three equivalent atop adsites (light blue in Fig. 5.1e) to anchor the CO (√3x√3)R30° pattern, thus spanning three equivalent overlayer sublattices. The facet edges consist of two alternating sets of three equivalent sides, much as any hexagonal fcc island is surrounded by steps with alternating (111) and (100) facets. One of the sets of sides is equally decorated with CO

molecules no matter which central substrate atom anchors the overlayer. Of the other set of sides, however, only two are covered intimately, leaving open space near the third side (yellow in Fig. 5.1e).

The open space can be avoided if the CO adlayer is imperfect: a dislocation line in the overlayer allows placement of adsorbates at all sides of the second set equivalently. Consequently, the confined adlayer is under competition between forming the structure found on extended surfaces and incorporation of a dislocation line that permits equal filling of the edge sites, i.e. providing optimal edge interaction at the expense of intermolecular interaction. In both cases, the same number of CO molecules fit onto the exposed facet. The observation of the persistence of the dislocation lines indicates that the interactions at the adlayer edge are dominant over those within the adlayer.

Imaging 75 setups of one dislocation line at 24 K, it is found that in ≈ 40% of the cases a kink is present in the line. A dislocation typically affects 16 molecules (8 per side); a kink in the double line increases this number by 2 along the dislocation line (Fig. 5.1g). Analyzing the measured fraction of kinked lines using the Boltzmann equation and taking into account the degeneracy of the various possible kinked configurations, a kink energy of 6.1 ± 0.3 meV and a total energetic cost of the entire dislocation line of ≈ 0.05 eV were estimated. For three molecules the edge-interaction is improved by the dislocation line (yellow in Fig. 5.1e). This yields a lower boundary of the edge interaction of ≈ 0.02 eV

per molecule, a considerable energy compared to, e.g., the CO diffusion barrier of 0.075 eV.[84]

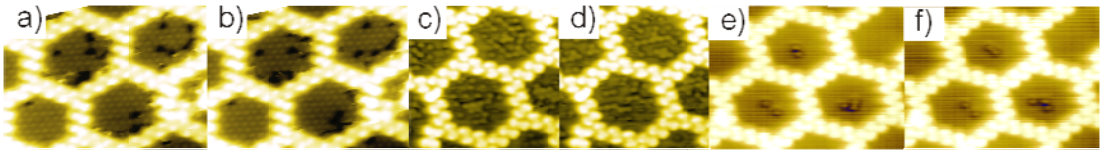

Figure 5.2 images from STM movies showing the diffusion of a,b) vacancies in a ($\sqrt{3}$x$\sqrt{3}$)R30° CO coverage in confinement (image parameters: 12 nm x 9 nm; Bias: -1.23 V; Current: 120 pA, Temperature: 23 K); c,d) 20-22 CO molecules on each exposed facet (image parameters: 8 nm x 8 nm; Bias: -0.72 V; Current: 60 pA, Temperature: 22 K); e,f) two and three CO molecules in confinement (image parameters: 12 nm x 9 nm; Bias: -2.67 V; Current: 100 pA, Temperature: 27 K).

The presence of the dislocation can potentially affect the chemical reactivity of the film markedly: molecules affected by a dislocation line have a nearest neighbor configuration that allows more ready access to them as well as the underlying substrate. The number of molecules affected by the dislocation scales linearly with the size of the facet, whereas the total number of molecules scales quadratically, indicating that the smaller the facet size, the more pronounced this effect. For the 4 nm facets studied here, more than ¼ of the adsorbates (16 out of 62) are directly affected by the dislocation line, significantly greater than on extended terraces.

The constant motion of the dislocation lines well below 30 K contrasts substantially with the behavior of individual CO molecules on Cu(111), whose diffusion starts only at $\approx$ 33K.[84] Is this effect limited to dislocation lines? Preparing films of

slightly lower coverage with facets that have a small number of vacancies in their ($\sqrt{3}$x$\sqrt{3}$)R30° coverage (Fig. 5.2a,b), rapid motion at similarly low temperature was observed. While increased diffusivity at high coverage has been observed in the past – to our knowledge it has not yet been quantified except at very low concentration[84] and for direct neighbors.[85, 116] [117] The confined nature of our exposed facets allows us to monitor the diffusion rate for a fixed number-density of molecules. The dotted line of Fig. 5.3 shows the diffusivity from a few molecules per pore (Fig. 5.2e,f) up to the point at which the ($\sqrt{3}$x$\sqrt{3}$)R30° adlayer is 1/3 complete and site blocking becomes important (Fig. 5.2c,d). While data points for coverages up to 6 molecules on the exposed facet were measured at 27 K, diffusion at higher coverages was too rapid at this temperature; the data point for 21 molecules per pore was measured at 22 K and scaled according to the Arrhenius parameters of Ref. [84]. The dotted line represents an exponential fit of the diffusivity.

A detailed look at the STM images indicates that the diffusivity depends not only on the number of molecules on the exposed facet but also on the position of the molecules within that facet. Generally, molecules tend to move less if they are closer to the center and more rapidly around the perimeter. Unfortunately, this renders a complete Arrhenius-based evaluation (which would need to separate molecules by location) beyond reasonable effort.

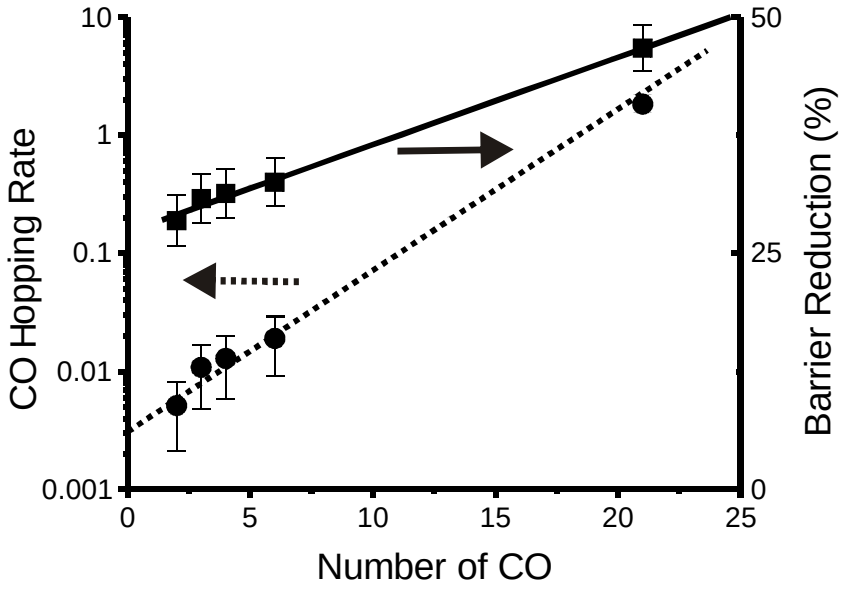

Figure 5.3 dotted line: diffusion rate per molecule as a function of number of molecules on an exposed facet; solid line: reduction of the diffusion barrier that causes this acceleration under the assumption of a constant diffusion prefactor. All error bars are dominated by the temperature uncertainty of 1 K in our measurements; the statistical error is much smaller than the data markers.

Thermally programmed desorption experiments showed that an increase of the surface coverage can lead to a reduction of the adsorption energy.[99] In the simplest approximation, the diffusion barrier is a constant fraction of the adsorption energy. While this argument justifies a variation of the diffusion barrier with coverage, it provides little indication that the diffusion preexponential factor should vary markedly with it. Fixing the diffusion prefactor at the value for isolated molecules,[84] the variation of the diffusion barrier with coverage can be obtained from the diffusion data (Fig. 5.3, solid line). The adsorption and subdivision of the Cu(111) terrace by the anthraquinone network causes a reduction of the CO diffusion barrier by ¼; increasing the coverage

inside the pore up to 1/3 of the (√3x√3)R30° adlayer reduces the diffusion barrier by another ¼. The data suggests a linear fit of the reduction of the barrier as a function of the coverage with a slope of (57 ± 14) %/ML, with 1 ML defined as the complete (√3x√3)R30° coverage. If the adsorption energy is assumed to be proportional to the diffusion barrier, then its reduction by half indicates a comparable reduction of the adsorption energy. The observation of a linear dependence of the energy reduction on the number density of molecules suggests that its origin is not direct pair interactions (which scale quadratically with coverage) but involves the substrate, potentially both through confinement-induced surface state effects[118-120] or through mediation of trio and higher order interactions.[121] While the effects of site blocking and nearest neighbor interactions prevent us from obtaining experimental data beyond 1/3 ML coverage, our results suggest a quite substantial destabilization of the CO molecules in the (√3x√3)R30° adlayer, well in line with the results discussed in Ref. [99, 117]

Following this discussion of the CO dynamics, coworkers and I finally examine the locations the molecules/vacancies occupy and the effect of the lateral confinement on them. To this end, the distribution of vacancies in coverages like the one shown in Fig. 5.2a-d and of molecules in coverages like shown in Fig. 5.2c,d were studied.

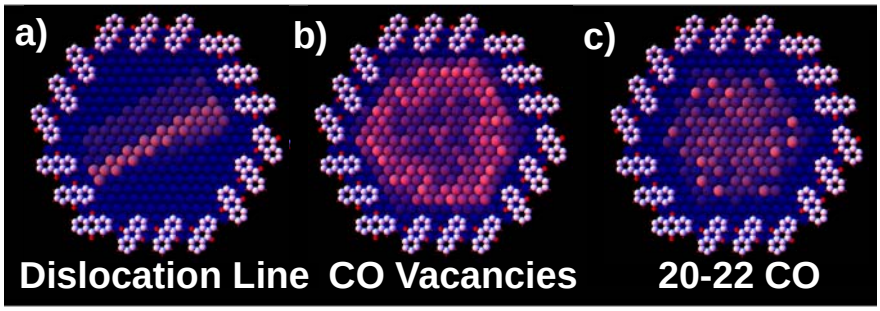

Figure 5.4 color coded histograms of CO vacancy/molecule distribution for each of the 186 Cu substrate atoms exposed within an anthraquinone pore. The anthraquinone pore is chiral and threefold symmetric, panels b) and c) are averaged over three equivalent rotational orientations. a) Dislocation lines are most commonly found to cross the facet center, b) whereas vacancies are more commonly found around the facet edge. c) For 20-22 CO molecules a relatively featureless distribution is observed. Each panel represents the location of >1000 vacancies/molecules.

Fig. 5.4a shows the likelihood that the dislocation line of Fig. 5.1b,c,d occupies different substrate sites in a color-coded histogram. In this context it is important to realize that although the anthraquinone network appears sixfold symmetric, due to the threefold (and not sixfold) symmetry of the substrate, every other of its sides comes to rest at different surface locations. The dislocation line generally crosses near the center of the exposed facet thereby connecting dissimilar edges. Consequently, the area showing higher occupation of the dislocation line in the center right of Fig. 5.4a is not equivalent to the area on the center left of the pore line. The sensitivity of the dislocation line to the geometry of the facet boundary is a testament to the importance of confinement for the spatial distribution of adsorbates.

Fig. 5.4b shows the distribution of vacancies on exposed facets a few molecules short of saturation; bright colors correspond to a high likelihood of finding vacancies. Viewing a large number of movies with coverages similar to Figs. 5.2a,b, it is qualitatively observed that the vacancies frequently arrange themselves in rows that originate at the facet edge and often bend back towards the same or an adjacent edge. In the histogram of Fig. 5.4b, this is reflected in a higher probability for vacancies to be found at the edges, with a slight preference for one kind of edge and vertex. It is important to realize that in our observation, the vacancies do not segregate from the adlayer, i.e. they do not form a closely covered area surrounded by empty space as on extended terraces.[115] Rather the vacancies are interspersed with the adlayer, affecting a far greater fraction of the adlayer molecules and potentially rendering the adlayer more reactive. A statistical analysis of vacancy motion is much more complicated than for adsorbate motion, as in the (√3x√3)R30° overlayer 'fractional' vacancies (corresponding to molecules adsorbed in antiphase) can combine and molecules can occasionally and intermittently adsorb closer than the √3 spacing, so that the total number of vacancies on an exposed facet is not conserved.

Reducing the coverage to 20-22 molecules on the exposed facet (i.e. ≈ 1/3 of the (√3x√3)R30° adlayer), aggregation into large islands was not observed (Fig. 5.2c,d). Despite the low temperature only small aggregates of molecules form, with almost every molecule being accessible on the surface from at least one side. This is, again, in marked

contrast to CO films on extended terraces, where extended (√3x√3)R30° islands under similar conditions were found.[115] The distribution of molecules within the exposed facet is relatively featureless; no preferred or avoided regions of adsites can be discerned (Fig. 5.4c).

5.4 Conclusion

Coworkers and I conducted a survey of the effects that nanometer-scale confinement can have on adsorbate dynamics and placement: on small exposed facets we found that adsorbate diffusion increases rather than decreases, resulting in more even and open distributions of adsorbates and adlayer vacancies than found on extended terraces. Even at full coverage, confinement can stabilize dislocation lines which affect a substantial fraction of the molecules in the adlayer (> ¼ of them). In combination, these findings suggest that confinement alone can increase the potential for surface reactivity in an adsorbate film: the smaller the facet size (i.e. the smaller a metal nanoparticle that creates it), the more pronounced the mentioned effect.

Chapter 6

CO adsorbates within nano scale pores on Cu(111)-Part2

(From publication: Physical Review Letters, 2010, 105, 066104)

6.1 Introduction

Understanding the adsorption of molecular species at solid surfaces resonates as one of the unifying themes throughout the evolution of surface science over the past half-century. The adsorption of an ever increasing number of molecules on crystallographic surfaces, as well as on steps and at other defect sites, has been studied. Great progress has been made in the development of computational techniques that reveal the electronic interaction between adsorbates and the underlying substrate atoms. However, the effect of lateral confinement of the support on the nanometer scale has remained largely unaddressed because of challenges in the preparation of surfaces covered with atomically identical patterns several nanometers in scale and because of computational limitations in simulating systems consisting of many hundreds of substrate and adsorbate atoms. Yet many of the applications of surface science, for instance in heterogeneous catalysis or in semiconductor processing, crucially rely on nanoscale-delimited surfaces; and recent progress in these fields emphasizing the effects of nanoscale confinement[122] and diminishing scale, respectively.

In this study coworkers and I address how confinement of the substrate to approximately 4 nm hexagons, i.e. larger than most adsorbate patterns[111, 120] and substrate unit cells but smaller than previously investigated structures such as quantum corrals and adislands,[118, 123] affects the distribution and energetics of small molecule adsorption.

It has been shown that perturbation of substrate electronic states, such as an underlying gas bubble[124] or scattering of a Shockley surface state at a step edge[125]or adatom row[126], affect adsorbate distribution. Substrate-mediated long range interactions between molecules have been found in a variety of systems and quantified in a number of cases.[27, 84, 105, 116, 127-133] A correlation between the location of CO molecules on Ag(111)[107] and benzene on Cu(111)[125] with the phases of the surface scattering amplitude have been proposed from experimental data and through theoretical modeling.[121, 134] In this experimental study coworkers and I show that confined electronic states of the substrate can actually be titrated with adsorbates, arguably much as electronic states are filled up from the lowest to highest energy in an atomic orbital diagram.

6.2 Experimental

Our measurements were conducted on a Cu(111) surface decorated with a chiral anthraquinone network of sixfold symmetric (disregarding the substrate) exhibiting pores

that expose 186 substrate atoms in their midst.[27] CO was used as our test molecule because a wealth of data on its surface behavior is available: CO molecules adsorb upright atop Cu(111) substrate atoms. They are imaged in scanning tunneling microscopy (STM) as protrusions or indentations, depending on whether the STM tip is decorated with a CO atom at its apex or not, respectively.[114] Sample preparation involves the usual sequence of sputtering and annealing, followed by cooling to liquid nitrogen temperatures. The anthraquinone pattern is created by evaporation of the molecule onto the cryogenic sample followed by annealing to room temperature. Deposition of CO molecules through a leak valve onto the anthraquinone-patterned surface at 40K preserves the pore shapes.

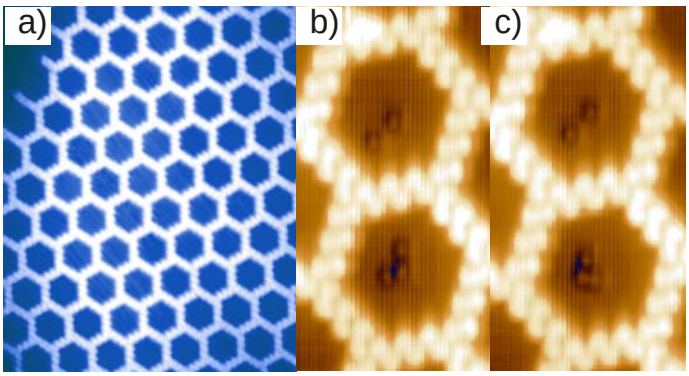

Figure 6.1 a) array of atomically defined pores on Cu(111) formed by deposition of anthraquinone according to Ref. [27] Image parameters: 38 nm x 43 nm; Bias: -2.534V; Current: 50 pA b,c) images from a movie showing the diffusion of two and three CO molecules in confinement. Image parameters: 6 nm x 10 nm; Bias: -2.673 V; Current: 99 pA.[135]

6.3 Results

It is found that the anthraquinone network blocks the diffusion of adsorbed CO molecules on the substrate; repeated imaging of the same set of pores allows tracking of the perambulation of a fixed number of molecular entities within a confined area. By watching diffusion of CO for long time, it is found that in each of which a few molecules are seen to diffuse. In such sequences of images each molecule can be assigned to a particular substrate atom on which it is adsorbed. From thousands of images obtained, histograms of the occupation of the various substrate sites within the confined area were calculated (Fig. 6.2a-e). Each confined area consists of 62 threefold degenerate (186 in total) adsites surrounding a hollow site at the pore center in a threefold symmetric arrangement. The anthraquinone network is chiral, preventing inversion symmetry.

The radial distribution of CO molecules in pores of different coverages is shown in Fig. 6.3a. Given the large number of different adsites, 7 radial bins were constructed, as indicated in the inset of Fig. 6.3a. In pores containing a single CO molecule, the CO is generally found at the pore center; in 54% of the cases, the molecule occupies one of the two inner bins of Fig. 6.3a. From the distribution of Fig. 6.2a, the radial variation of the probability P_i of CO occupation of an adsite i indicated in the yellow (front) curve of Fig was obtatined. 6.3a. From this dataset coworkers and I can construct the canonical partition function Z of the single CO system, which allows us to deduce the radial variation of the CO adsorption energy ε (Fig. 6.3a).

$$Z = \sum_i e^{-\varepsilon_i / kT} \quad with \quad P_i = e^{-\varepsilon_i / kT} / Z$$

with k the Boltzmann constant and T the temperature 27 K of our measurements . The resultant variation of ≈ 14 meV is quite substantial, approximately 1/5 of the CO/Cu(111) diffusion barrier of 75 meV.[84]

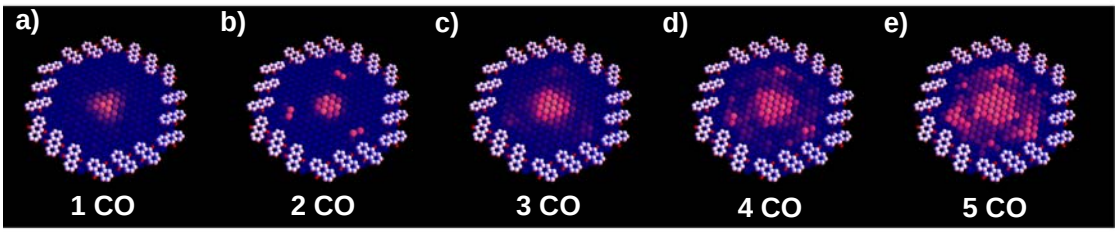

Figure 6.2 Color coded plots of the probability of CO molecule occupation for each of the 186 Cu substrate atoms exposed within an anthraquinone pore. Each plot is based on > 500 CO configurations observed and averaged over equivalent locations.

For two CO molecules in the system (Fig. 6.2b), it is generally found that either both molecules occupy the confinement center or they are split between the center sites and a set of three equivalent adsites approximately half-way towards one set of confinement vertices. The same set of three adsites is also favored in pores that contain 3-5 molecules (Fig. 6.2c-e). Experimentally, these are independent datasets acquired on different pores, days and sample preparations; the reappearance of the same location for pores of different coverage rules out experimental error (e.g. through subsurface defects) as the origin of the peripheral peaks in Fig. 6.2. This poses the question of their physical origin and, in particular the reason for their threefold symmetry. The ≈ 4nm diameter of

the pore rules out direct intermolecular interactions, suggesting that a substrate-mediated effect may be of relevance. Unfortunately, first-principles computational methods (such as density functional theory) are incapable of treating a system that requires at least 186 substrate atoms per layer (i.e. several hundred in total). Thus, coworkers and I resort to a continuum model of the substrate electronic setup focusing on the Cu(111) surface state. In this context it is important to realize that although the pore boundary itself is sixfold symmetric, the pore vertices are alternatingly centered on hcp and fcc hollow sites, so that the overall symmetry of the pore on the substrate has the same threefold (and not sixfold) symmetry of the CO distribution.(Fig. 6.2.) Thus, the confined electronic states within the pore were calculated starting from the known solutions of a particle in a triangular box[135], followed by relaxation into the actual geometry of the pore.

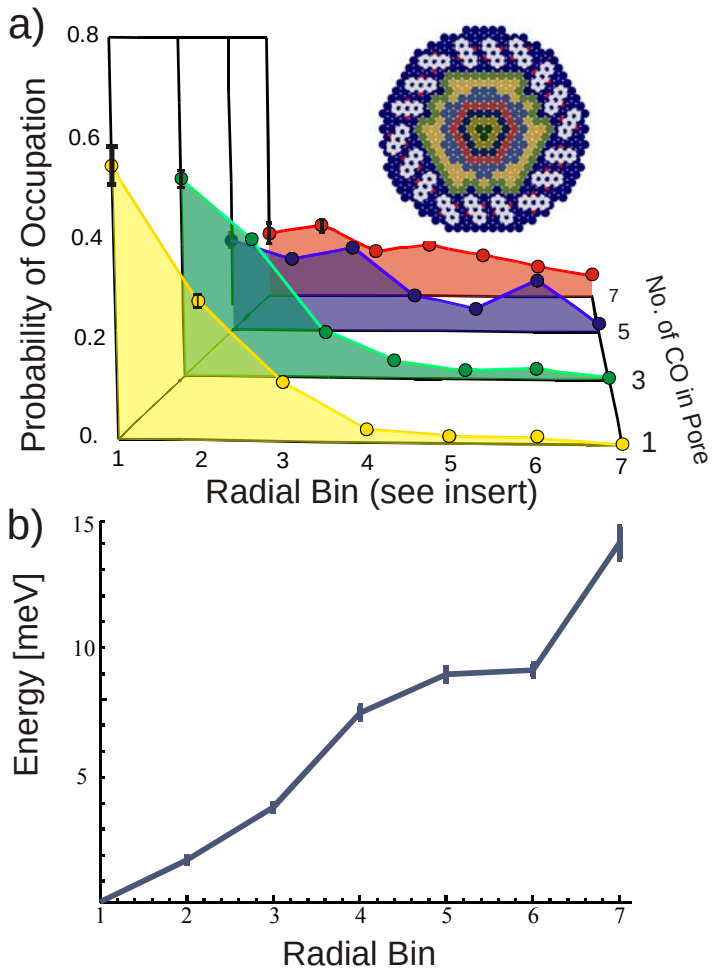

Figure 6.3 a) normalized probability of occupation of radial bins (shown in the inset) for pores containing 1-7 molecules. For 1,3 molecules the distribution is monotonic, whereas at increasing number of molecules also an additional intermediate distance becomes favored until further increase of the coverage renders the plot featureless. b) Variation of the adsorption energy of a single CO molecule across a pore. Error bars are based on √counts in the histogram and are shown in panels a,b when larger than the data markers.

Gross et al. showed that scattering of the surface state from organic molecules occurs not at the peripheral hydrogen atoms but at the 2nd period elements.[136] Hence, coworkers and I construct the boundary of our pore from the six carbon and oxygen

atoms per molecule (102 in total) that are closest to the pore center. We adapt an iterative finite-difference algorithm[137], more commonly used for solution of Poisson or heat-diffusion equations, to the relaxation of the known solutions into the geometry of the pore. Here, we develop the wave function in a Taylor series to third order; summing over four locations adjacent to a point (x,y) reproduces the Hamiltonian H_{inside} inside the potential-free pore.

$$\frac{\langle x+\delta, y| + \langle x-\delta, y| + \langle x, y+\delta| + \langle x, y-\delta|}{\delta^2}|\varphi\rangle - \frac{4\langle x, y|\varphi\rangle}{\delta^2} \cong \frac{-2m^*}{\hbar^2} H_{inside}|\varphi\rangle = \frac{-2m^*}{\hbar^2} E|\varphi\rangle$$

with m* the effective mass of an electron of the surface state of 0.34 electron masses and

a small displacement. Thus, if φ_{n-1} is an approximate eigenfunction of the Hamiltonian, a better approximation φ_n can be found by evaluating

$$\langle x, y|\varphi_n\rangle = \frac{\langle x+\delta, y| + \langle x-\delta, y| + \langle x, y+\delta| + \langle x, y-\delta|}{4 - 2m^*\delta^2 E_{n-1}/\hbar^2}|\varphi_{n-1}\rangle$$

Alternating this iteration and Gram-Schmidt orthogonalization[138] of the set of eigenfunctions originally obtained from the triangular particle in the box problem, we end up with three eigenfunctions (one unique and one twofold degenerate) whose eigenvalues E of 170 meV and 440 meV, respectively, are below the Fermi Energy E_F, if measured from the bottom of the surface state band of 450 meV below E_F.[119, 139] Fig. 6.4a,b shows the distribution density of state associated with the first and twofold-degenerate second state, respectively. Our algorithm provides correct eigenfunctions and –states that

are converged and invariant to the grid spacing of 1.25 Å, 0.63 Å, or 0.41 Å (corresponding to using a 40x40, 80x80 or 120x120 points grid to represent the pore); however, it cannot guarantee completeness of the set of eigenfunctions/-values found. Summation of the fraction of the surface Brillouin zone filled by the surface state (characterized by the Fermi vector $k_F = 0.21$ Å^{-1})[139, 140] over the exposed substrate atoms leads to no more than 3 complete electron pairs in the surface state within each pore, in good agreement with the three states found. This result is further corroborated by the recent finding of Lobo-Checa et al. by electron spectroscopy that in a molecular surface network of roughly 1/3 the size of our system there is exactly one confined state.[120]

Comparison between the density of state of Fig. 6.4 and the molecular distribution within the pore of Fig. 6.2 reveals a remarkable correspondence. Moreover, the sequence of lateral arrangements of CO molecules found when 'titrating' the pore with an increased number of molecules, i.e. first filling the pore center and subsequently the peripheral states, matches the energetic order of the surface state density of states so that the filling of CO molecules into the pore is reminiscent of filling electrons into an atomic orbital diagram. While previous work on the interaction of adsorbates with the surface state focused on comparison with the lateral surface state distribution at E_F visible in STM, the energy integrated approach afforded by the small scale of the pore provides a much more complete understanding of the underlying physics.

Increasing the number of molecules inside the pore beyond the number of electrons in the surface state (i.e. 6) causes the radial distribution of molecules in the pore to become more uniform (red curve in Fig. 6.3a), showing the limitation in adsorbate guidance achievable in a pore of given size. This finding corresponds with CO's ability of quenching the surface state at relatively low coverage.

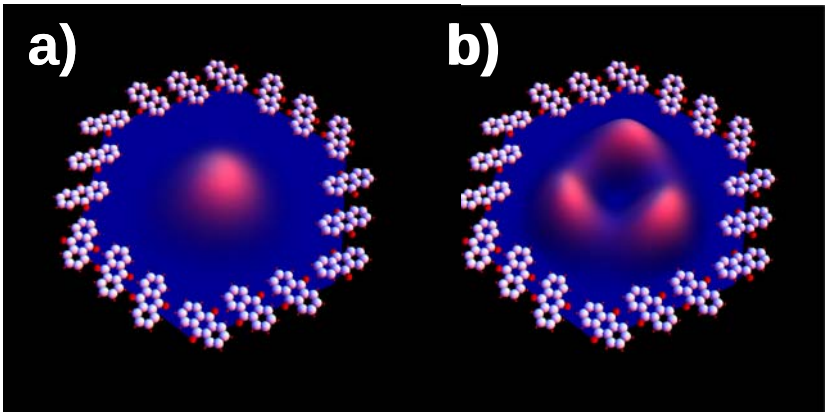

Figure 6.4 a,b) Plot of the local density of states of the first and twofold-degenerate second electronic state of the pore, respectively. Compare to the distribution of molecules in pores in Fig. 6.2.

Although our calculations were based on free-electron-like behavior of the surface state electrons (i.e. a constant potential within the pore boundary) with just an effective mass accounting for the presence of the substrate, our finding of threefold symmetry (as enforced by the substrate, in contrast to the sixfold symmetry of the molecular network) is crucial for explaining the experimental distribution of adsorbates; this highlights the limitation of the free electron approximation in understanding surface state electrons and their impact on adsorption.

6.4 Conclusion

By monitoring adsorbate diffusion within a nanometer-scale confined system it is found that such confinement has a pronounced effect on their average location, suggesting that engineering of confinement boundaries may not only allow engineering of surface electronic states but can also be a tool in assembling molecular patterns at surfaces.

Chapter 7

Elastic properties of a molecular monolayer on Cu(111)

(From publication: Physical Review B, 2010, 32, 201410)

7.1 Introduction

Understanding how materials respond to stress and, subsequently, having the ability to predict the resultant deformation (strain) are fundamental to virtually all practical applications of materials. In depth understanding of material-specific stress-strain relationships is of consequence to a wide range of scientific fields as varied as the geological deformation of rock[141] in the course of plate tectonics and the posture-induced deformation of lumbar disks resulting in herniation.[142] It also has significance for applications at the nanoscale; for example in the development of molecular-scale coatings, knowledge of the elastic properties of the employed materials is essential for prediction of their ability to maintain integrity under the deformation of their substrate. Yet investigations of molecular overlayers at solid surfaces have generally not addressed issues related to the elastic properties of films, with a few exceptions as in cantilever measurements of magnetostriction.[143-145] Currently the formation of molecular networks at metal surfaces garners significant attention, because they permit patterns of unprecedented size and versatility.[9, 27, 41, 46, 111] The present study aims at

complementing the advances in creating molecular surface patterns with the development of a framework for understanding their elastic properties.

7.2 Experimental

The focus of this study is a system that was chosen because of the simplicity of the geometry of its components and of their interaction with one another: anthracene on Cu(111). Anthracene consists of three fused benzene rings (Fig. 7.1 inset) and adsorbs flat on Cu(111) similar to other acenes.[129, 146-150] Dispersive or van der Waals (vdW) interactions play an important role in adsorption of acenes (such as benzene) on low-corrugation metal surfaces. In a prior study[91] Berland, K et. Al. addressed the physisorption of benzene and found that with density functional theory (DFT) calculations in the generalized gradient approximation, a negligible adsorption energy of ≈ 20 meV results,[151] which favors a hollow-centered ring over a bridge centered one by ≈ 5 meV . In contrast, in first-principles DFT calculations accounting for vdW interactions,[152] markedly-higher adsorption energies of 0.55eV and 0.53eV at hollow and top site, respectively, are found. Coworkers and I extend such calculations to anthracene on Cu(111) and find substantially higher binding energies of 0.95eV and 0.93eV, respectively (see Fig. 7.1a,b). There is a similar difference in adsorption energy ≈ 0.02 eV, i.e. less than anticipated from linear increase with the number of aromatic rings suggested previously.[153, 154]

In this study we address anthracene coverages on Cu(111) that are complete: no bare surface areas remain. We find a large range of adsorbate superstructures which distinguish themselves in geometry, fraction of molecules adsorbed at hollow vs. bridge sites and total coverage. In particular, our measurements show that higher coverage leads to an increasing fraction of the molecules in less favorable adsites. We show that this reduction in average adsorption energy with lateral compression can be interpreted as elastic behavior of the monomolecular film.

Sample preparation involved the typical cycles of sputtering and annealing followed by a sequence of cooling of the bare surface to ≈ 80K and deposition of anthracene through a leak valve. All measurements were performed in a low-temperature scanning tunneling microscopy (STM) chamber built on site. Modeling of the adsorption of anthracene involves a non-self-consistent approach in which the RPBE functional[155] was used self-consistently to obtain electron densities, which were then used to evaluate the nonlocal correlation energies using a first principle DFT treatment accounting for vdW interactions.[152] All calculations use the projector augmented wave method[156] implemented in the grid-based real-space code GPAW.[157] The supercell was modeled with a 5x5 Cu(111) slab of 5 layers topped by 21Å of vacuum, and an anthracene molecule placed parallel to the Cu(111) surfaces. The Brillouin zone was sampled only at the Γ point. Wave functions, electron densities, and potentials were represented on a 0.16Å real-space grid. We calculated the adsorption of anthracene at a hollow and at a

bridge site finding (besides the mentioned difference in energy) a small difference in the average height of the molecule's carbon atoms above the top-layer substrate atoms of 3.49 Å vs. 3.52 Å. In addition to the adsorption geometries discussed above and shown in Fig. 7.1a-b, we investigated a set of alternate configurations which, however, turned out to have prohibitively high energies.

7.3 Results

7.3.1 STM Study

Despite the relative simplicity of the adsorption system, highly polymorphic patterns, many of which are characterized by large and complex unit cells were found. Fig. 7.1c shows as an example a $\begin{pmatrix} 10 & 0 \\ -8 & 17 \end{pmatrix}$ superstructure with a unit-cell area of 957 $Å^2$ corresponding to 170 substrate atoms. Given 11 molecules per unit cell, not every molecule in the unit cell interacts directly with every other; consequently, it may be useful to describe the unit cells in terms of the underlying geometric motif that contains the intermolecular geometry. Fig. 7.1c highlights how in this superstructure six molecules surround a seventh one in a shape that resembles a 'fish'. Both the central molecules and one of the 'fin' molecules adsorb at less favorable bridge sites, with the remaining molecules adsorbing at the optimal hollow sites. The unit cell consist of a 'fish' shape and an 'anti-fish' shape (with a few shared molecules) connected by a glide reflection

line. In total, coworkers and I can identify five different surface patterns all of which can be found on the same sample in the same preparation.

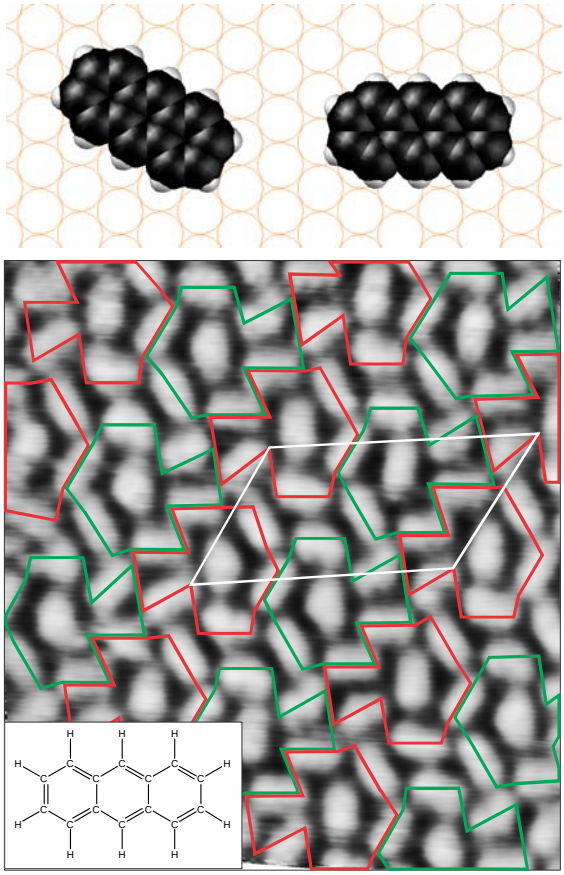

Figure 7.1 Adsorption configuration of anthracene on Cu(111) a) at a hollow site and b) at a bridge site. Each adsorption configuration is threefold rotational degenerate. Panel c) shows an STM image of an anthracene superstructure. The unit cell is indicated as a white parallelogram. The superstructure can be described by a geometric motif resembling a fish and its reflection (red and green shapes). The inset shows a chemical formula of anthracene. Imaging parameters: Current = 20 pA, Bias = -3.1 V, Size = 90 Å × 100 Å.

The $\begin{pmatrix} 4 & -1 \\ 1 & 4 \end{pmatrix}$ superstructure, shown in Fig. 7.2a, is the least dense one observed; its unit cell contains only one molecule, which is adsorbed at a hollow site. All molecules

are aligned in parallel and are adsorb at equivalent adsites. There are 17 substrate atoms in the unit cell for a coverage of 1/17 ML = 0.059 ML, with the monolayer (ML) referred to the substrate atom density.

Fig. 7.2b shows a $\begin{pmatrix} 12 & -4 \\ -8 & 12 \end{pmatrix}$ superstructure with a unit-cell size of 631 Å^2, in which six molecules form a symmetric hexagon surrounding a seventh; similar to the structures of Fig. 7.1c and Fig. 7.2 c-d, the surrounded molecule is adsorbed at a bridge site. The density of this film is 16 substrate atoms per molecule, corresponding to a coverage of 0.0625 ML.

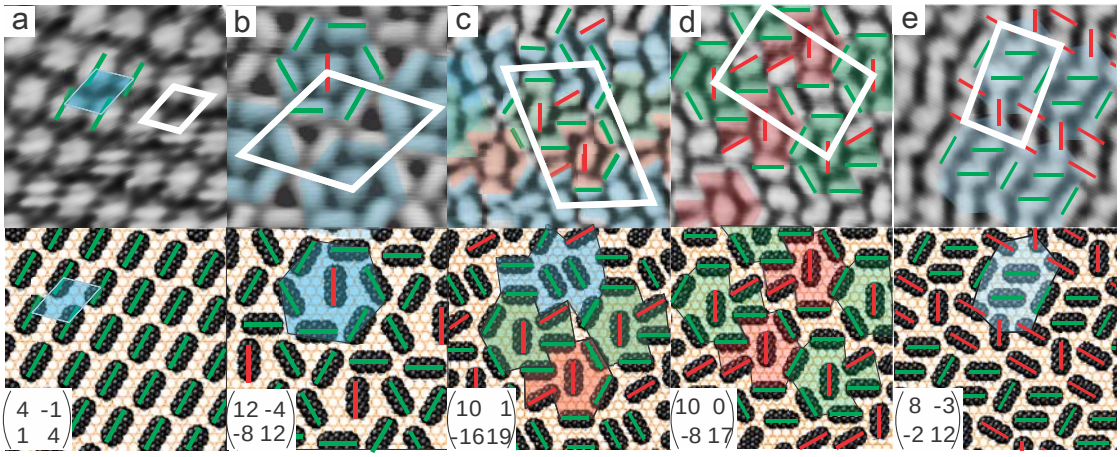

Figure 7.2 a-e) STM images and scaled models of anthracene coverages on Cu(111). The unit cells are indicated white and structural motifs are highlighted in color. Molecules adsorbed at hollow and bridge sites are labeled with green and red bars, respectively. Panels a,b) 54 Å × 54 Å, Panels c-e) 61 Å × 61 Å, Image parameters: a) Current = 18 pA,

Bias = -2.1 V, b) Current = 19 pA, Bias = -2.6 V, c) Current = 20 pA, Bias = -3.1 V, d) Current = 20 pA, Bias = -3.1 V, e) Current = 11 pA, Bias = -1.6 V

The $\begin{pmatrix} 10 & 1 \\ -16 & 19 \end{pmatrix}$ superstructure of Fig. 7.2c consists of rows of the fish motif of Fig. 7.1c arranged in a head-to-tail fashion; between these rows two parallel molecules are found adsorbed at the optimal hollow site. At a size of 1159.9 $Å^2$ the unit cell comprises 13 molecules, of which 9 come to rest on optimal hollow adsites. The coverage is 0.0631 ML.

Fig. 7.2d repeats the superstructure of Fig. 7.1c; it corresponds to a coverage of 0.065 ML. Finally Fig. 7.2e shows a $\begin{pmatrix} 8 & -2 \\ -3 & 12 \end{pmatrix}$ superstructure with a unit cell size of 507 $Å^2$ that features alternating bands of molecules adsorbed at hollow and bridge sites at equal numbers. There are 6 molecules in each unit cell for a total coverage of 0.067 ML, the densest coverage observed.

In total, five different phases that span a compression of the surface area per molecule by more than 10% were observed. The broad geometric diversity of the surface patterns may appear astonishing; however, similar observations have been made in the study of the statistical mechanics of granular media, even as conventional ones as

Basmati rice spread out on a vibrating plate.[158] Bates and Frenken showed that if spherocylindrical particles with an aspect ratios not exceeding 1:5 are confined in plane, then phases with a variety of local orders exist; at larger aspect ratios, a nematic phase becomes favored.[159] In contrast to the granular systems of Ref. [158], however, it is observed that these patterns always fill the entire space available, i.e. that they correspond to maximum expansion of the system and, thus, its equilibrium under the given confinement. The absence of coexistence of dense with less dense patterns suggests a driving force for expansion of the film, at least up to the most open coverage coworkers and I observe (Fig. 7.2a) corresponding to optimal adsorption configuration of all anthracene molecules. This invites the questions: a) what is the character of this restoring force is? and b) can it be understood in terms of continuum elastic theory?

7.3.2 Density Functional Theory Calculation

In the different superstructures a varying fraction (0% - 50%) of molecules occupy the energetically less-favorable bridge adsorption site. Fig. 7.3a plots the average adsorption energy per molecule as a function of coverage, revealing a monotonic relationship between the two. Based on the different anthracene adsorption heights at the bridge and hollow sites, the average film thickness was calculated (subtracting ½ of the copper interlayer spacing), which scales linearly with average adsorption energy (Fig. 7.3a) and increases with compression. Thus, conceptually it is found that as the film is

compressed from the coverage of Fig. 7.2a (in which each molecule attains its optimal adsorption position), its total energy rises and its thickness increases.

In the study of the mechanical properties of materials, it is common to plot the strain energy density (i.e. the total deformation energy per unit volume) as a function of the strain. Fig. 7.3b replots the dataset of Fig. 7.3a in this fashion. For an isotropic material subjected to stress in one plain the stress-strain relationship can be expressed as follows:

$$\sigma_{ij} = \frac{E}{1+\nu}\left(\varepsilon_{ij} + \frac{\nu}{1-2\nu}\varepsilon_{kk}\delta_{ij}\right)$$

in which E is the Young's modulus, σ the stress, ε the strain, υ the Poisson's ratio, δ the Kronecker delta and i, j, k denote the three spatial directions for which the typical summation convention is applied. For simplicity the anthracene films were regarded as isotropic. Based on the vertical expansion of the film shown in Fig. 7.3a, υ = 0.095 ± 0.006 for all but the least compressed films was calculated. For a material with a Hookean response, the strain energy density U, i.e. the compression work per unit volume, is $U = \frac{1}{2}\sigma_{ij}\varepsilon_{ij}$; for the particular case of an isotropic medium subjected to compressive stress in one plane yet free to expand normal to the plane, U simplifies to:

$$U = \frac{E(1-\nu)}{1-2\nu}\varepsilon^2$$

That is, the strain energy increases quadratically with the strain. A quadratic fit of the dataset of Fig. 7.3b yields a value of the Young's modulus of the molecular monolayer of

1.5 GPa, which is substantially less rigid than anthracene crystals (8.4 GPa) or copper (124 GPa).[160]

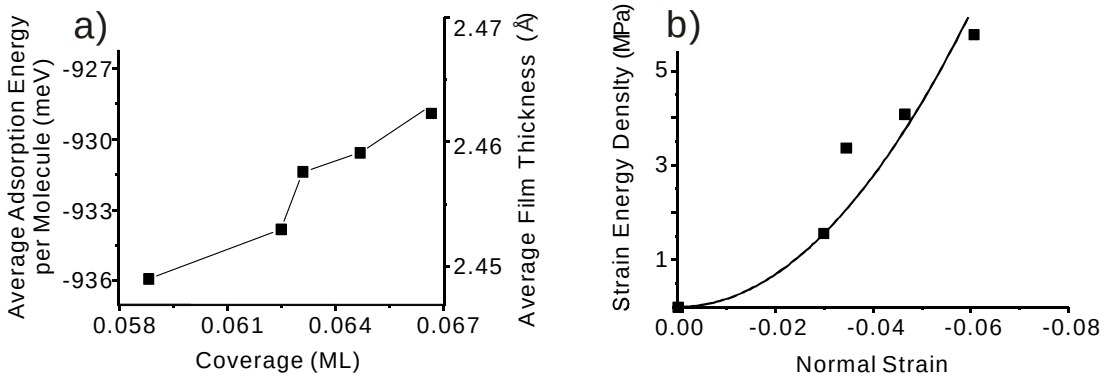

Figure 7.3 a) variation of the average adsorption energy per molecule and of the average thickness of the anthracene monolayer with coverage; b) strain energy density obtained from panel a) as a function of the compressive strain. The quadratic fit yields a Young's modulus of 1.5 GPa.

A combination of Young's modulus and Poisson ratio completely describes the elastic properties of a homogeneous isotropic material. How can the obtained values be interpreted? Low Poisson ratios, like the one observed here, are commonly found in porous materials where lateral compression is mainly adsorbed in reduction of pore volume rather than requiring transverse expansion of the object. If a porous material is deformed, a relatively small amount of matter has to deform compared to the overall volume of the object, and a relatively low Young's modulus results. This is also found here, suggesting that the closer packing of the molecules observed in our STM experiments can indeed be interpreted as compression of a porous material, revealing a

remarkable congruence of macroscopic and microscopic behavior. Note that the anthracene molecules are treated as hard, non-interacting particles; the interactions evaluated here stem exclusively from the variation of the vdW interaction of anthracene across the substrate.

7.4 Conclusion

Coworkers and I investigated the adsorption geometry of anthracene on Cu(111) and found – despite the adsorption system's comparative simplicity – a large number of highly-ordered superstructures with coverage varying by >10%. The polymorphic nature of the anthracene film coincides with the behavior of macroscopic granular media of similar aspect ratio. Modeling of the adsorption behavior of the system in first-principles DFT with account of vdW interactions, provides us with parameters which we use further to evaluate properties of the superstructures in terms of continuum elastic theory. Based exclusively on the lateral variation of the vdW interactions between the adsorbates and the substrate, the monolayer turns out to have ≈ 20% of the Young's modulus of the molecular bulk and a Poisson ratio of ≈ 0.1.

Chapter 8

Single layer of MoS_2 clusters on Cu (111)

8.1 Introduction

Recent research in the formation of atomically thin layers of van der Waals bonded solids by mechanical exfoliation have shown important new possibilities for the investigation of two-dimensional systems.[161] As an example, single-layer graphene show many unique physical properties which is not found in its layered structure, graphite.[162] This finding has opened up an entire new research field which was recently honored with the Nobel Prize in Physics. While graphene has many properties that make it an interesting candidate for microelectronic applications, such as its high carrier mobility,[163] high thermal conductivity[164, 165] and long carrier scattering lengths,[166-168] there are also aspects that offer challenges, such as the drop in its electron mobility when doped and its lack of a band gap[169, 170]. Atomically thin films of Molybdenum disulfide (MoS_2) are in many ways analogous to graphene, but they exhibit a significant gap (and, correspondingly, a different dispersion relation). The existence of a (direct) gap endows atomically thin MoS_2 with fundamentally different characteristics compared to graphene. The gap also implies the possibility of producing

field-effect transistors with very high on/off ratios, something that cannot be achieved in single-layer graphene. While MoS_2 and graphene show this important fundamental difference in electronic structure, the materials share some other common attributes related to the their stability as atomically thin films. In particular, one can: (1) obtain high levels of doping in the materials and large shifts in the Fermi energy by electrostatic gating; (2) produce and sustain very strong electric fields across the samples (with modest applied voltages); (3) produce very high levels of strain by simple means; (4) tailor the inherent properties of the material by changes in the surrounding media, through dielectric screening, doping effects, and changes in scattering channels; (5) produce composite materials by controlled deposition with other layered media; (6) produce free-standing, atomically thin membranes; and (7) explore a family of materials with related, but distinct properties as a function of defined layer thickness. In view of these factors, we anticipate that stable, atomically thin materials other than graphene – as exemplified by MoS_2 – will generate panoply of important advances in both science and technology.

However, the formation of atomically thin molybdenum disulfide was only achieved by a mechanical exfoliation method[171, 172] or H_2S gas exposure with vapor of molybdenum metal on gold surface.[173] Since liquid TEOS (tetraethyl-orthosilicate) is much preferred and less dangerous to handle than gaseous silane, it is chosen for many CVD process. In the same manner, a liquid sulfur source is favored for industrial

application. In this study, benzenethiol on Cu(111) was used as a sulfur source, rather than the H_2S gas required for the growth on gold.[173] In contrast to gold, copper forms a surface sulfide and, thus, can store the sulfur required for the subsequent MoS_2 formation. After the sulfur preloaded copper surface is prepared by benzenethiol, molybdenum was deposited separately using a metal evaporator. By this method, the growth of atomically thin two-dimensional molybdenum disulfide film on Cu(111) was successfully observed.

8.2 Experimental

We use a home-built variable-temperature scanning tunneling microscope (STM) operated in ultra-high vacuum. Cu(111) sample preparation involved sputtering (Ar+, 3 kV) and annealing of a single crystal followed by cooling to liquid nitrogen temperatures within the STM. Deposition of benzenethiol onto the cold sample occurred from a glass capillary attached to the vacuum chamber through a gate valve in a line-of-sight fashion while controlling the deposition rate through measurement of the pressure in the vacuum chamber. After deposition, the copper sample was annealed to more than 100°C, which is previously reported as a dissociation temperature of benzenethiol[174], to leave sulfur only on Cu(111) surface. While annealing, the increase of benzene peak (a fragment of bezenethiol) was detected by a mass spectrometer and it continued until no significant benzene peak shows. Figure 8.1 shows three patterns of sulfur on Cu(111) obtained through this method, which have well known geometry.[175-177] No remnant of carbon is present, and films grown with benzenethiol are identical to ones grown via H_2S.

Multiple cycles of exposure to benzenethiol and subsequent annealing allow almost arbitrary loading of the surface layer by sulfur. Consequently, molybdenum was deposited using a surface-science style commercial e-beam evaporator (Omicron) in various deposition rates but no more than 1 monolayer and dosing time of 10min to 6 hours to examine the relationship between deposition rate and ordered MoS_2 forming. Sample was annealed more than 500°C after molybdenum deposition so that the adsorbates have sufficient energy to move about the surface.

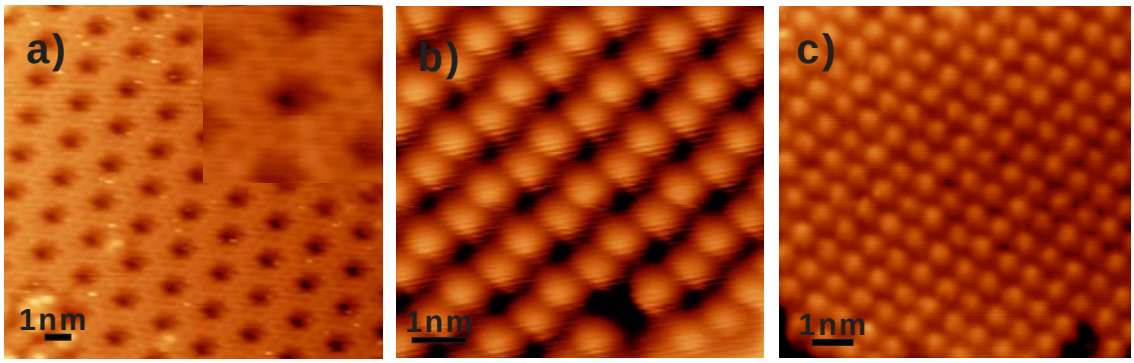

8.1 Figure a) STM images of a) hc structure with a $\begin{pmatrix} 7 & 1 \\ -1 & 6 \end{pmatrix}$ of matrix notation. b) zigzag structure with a $\begin{pmatrix} 3 & 1 \\ -2 & 5 \end{pmatrix}$ of matrix notation. c) triangle structure a $\begin{pmatrix} 4 & 1 \\ -1 & 4 \end{pmatrix}$ of matrix notation.

8.3 Results

Three different patterns of sulfur structures are observed and used in this study as substrates for the formation of sulfided molybdenum clusters. Increase of the benzenethiol coverage leads to the formation of hp structure(Fig. 8.1a) followed by the

formation of a zigzag structure(Fig. 8.1b) and hexagonal structure(Fig. 8.1c), that is described in matrix notation as $\begin{pmatrix} 7 & 1 \\ -1 & 6 \end{pmatrix}$, $\begin{pmatrix} 3 & 1 \\ -2 & 5 \end{pmatrix}$ and $\begin{pmatrix} 4 & 1 \\ -1 & 4 \end{pmatrix}$, respectively, and the density of sulfur increases from a) to c) in the coverage of 0.28~0.43.[175, 177] Molybdenum is deposited on these three sulfur patterned layers. There was no different structure of sulfur patterns observed before the deposition of molybdenum and these different patterns doesn't affect the structure of sulfide molybdenum structure. It seems sulfur layers serves as a sulfur source only regardless of their structure. After small amount of molybdenum deposited at high flux of Mo source (0.2Å/min), there were no sulfur pattern changes observed but it is clearly observed that some of the clusters absorb nearby sulfur atoms and form sulfided molybdenum islands(Fig 8.2 a,b). mono and bilayer of sulfided molybdenum clusters are formed but the size of most islands limits to less than 20nm^2, which implies that the spontaneous aggregation unlikely occur even through 500°C of annealing at this low coverage. In the previous study of single layer of MoS_2 on Au(111),[173] it is reported that the triangle structure of MoS_2 clusters is dominant than hexagonal and truncated hexagonal structures. However, in this experiment on Cu(111) the triangle structure is more dominantly observed at small size of MoS_2 clusters (less than 16nm^2) and when the cluster forms in the large size, the majority of clusters are seen to be hexagonal, truncated hexagonal structures and even the polygon structures, in which the side of edge is still parallel to the sixfold symmetry of substrate copper lattice. The existence of these structures has been speculated previously,[178] and it might seem that clusters have more chance to adopt the most

stable edge termination since free energies of molybdenum and sulfur have equal stability as in triangle structure as the size of cluster gets bigger. The height of clusters are determined from STM line scans and for the monolayer one, 3.22±0.1Å was measured, which is closed to the geometrical distance of 3.16Å from bottom sulfur layer to top sulfur of the MoS_2 single layer slab. To grow the cluster size, more molybdenum was deposited in the same condition and the formation of bigger clusters was observed.(Fig. 8.2.c) Additionally, more surface sulfur atoms participate in the forming of sulfided molybdenum clusters; consequently, the initial sulfur pattern disappears and bare copper surface comes into sight. In some areas, the hp structure appears, that is, the least dense sulfur structure. The height of clusters are mearsured again with the same method mentioned above and the formation of monolyaer and bilayer was observed. For bilayer structures, the value of 8.61±0.5Å was measured, which indicates a layered compound, consisting of stacks of S-Mo-S sandwiches held together by van der Waals interactions. However, this is slightly smaller value of one measured from bulk structure of MoS_2 (9.24Å), which could be an indication of the substrate effects to the layered structure. This will be discussed with Fig. 8.4 below.

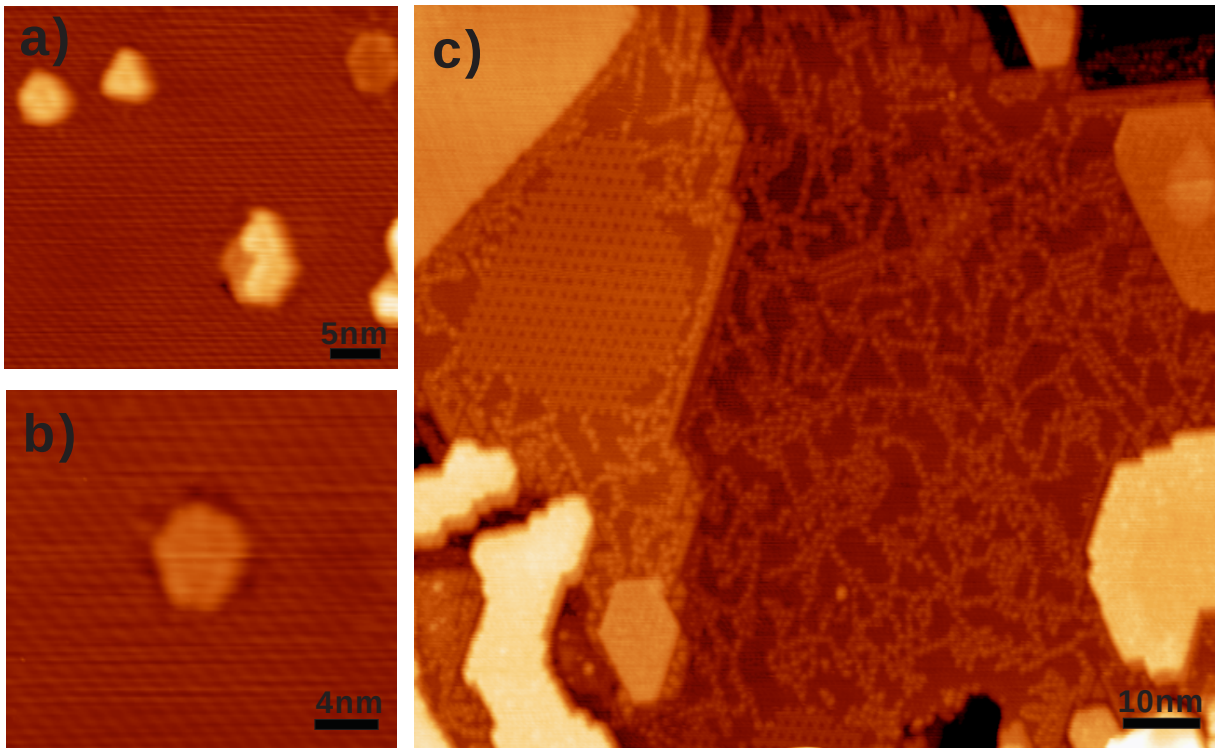

8.2 a) An STM image of MoS_2 clusters with various structures (triangle, hexagon, truncated hexagon). b) MoS_2 cluster absorbed nearby sulfurs. c) An image obtained after more molybdenum deposited from a) and b). It shows that lager clusters of truncated hexagon and polygon structure are formed.

To know the dependence of deposition rate to layer thickness, low flux deposition of molybdenum was performed to compare with the previous high flux experiment and we observed that the formation of monolayer clusters are favored in this low deposition rate. At this deposition condition, sulfur preloaded Cu(111) sample is exposed to RT for more than 4 hours. This may be the reason why monolayer clusters are more favorable to form than thicker layers. However, this should not be interpreted as an evidence to evaluate the kinetic process of this growth mode. To get more information on the relationship between flux and duration of deposition, we performed similar experiments

by changing only deposition parameters between these two low and high fluxes but no remarkable evidence was found. However, it is noted that we have more chance to get monolayer sulfided molybdenum clusters than thicker ones. To understand this, future study is required. Currently, Bartels' group is building a new UHV system, which has a capability of UPS/XPS/ISS study and this whole system will be designed to be mountable to a current STM system so that it allows additional spectroscopic measurements along with STM experiment. This will give us another chance to investigate the formation of MoS_2 clusters quantitatively in the near future.

With this low flux of molybdenum deposition, we deposited molybdenum several times by monitoring cluster formation step by step. As this process was repeated, less sulfur atoms remained on the surface and no more sulfided molybdenum clusters could be grown. At this point, we deposited more benzenethiol as a sulfur source to recover the initial sulfur fully-loaded condition. The pre-loaded sulfided molybdenum clusters are not significantly affected by this second sulfur loading process, which means benzene fragment from annealing process doesn't react with molybdenum. After several repeated procedures, many and various structures of single layer molybdenum clusters could be observed. (Fig. 8.3) Additionally, new pattern of sulfur structures appears followed by the deposition of molybdenum. This structure is previously reported but not intensively studied.[175] This structure will be discussed separately from this study with a combined DFT study later. Fig.8.4 shows the well-decorated single layer of molybdenum disulfided

island. Figure 8.4a) is a 3D rendered STM images and b) is the high resolution 2D image of the boxed area of the left image. The pattern on the top of the islands observed is the same as the sulfur pattern in the MoS_2 layer but the measured spacing between two sulfurs is 2nm, which is more than six times larger than the geometrical distance of 3.16Å. According to the work of Tersoff and Hamann, the tunneling current is proportional to the local density of states at the surface.[179] It has been reported many times that Moire patterns observed in STM images are larger than the geometrical structure by up to 31 times in layer materials such as graphene,[180-182] graphite[183-187] and transition-metal dichalcogenides.[188, 189] In these materials, interlayer interaction is very weak and, therefore, the influence of substrates to the overlayers would be significant. It is possible that charges in the electronic structure below the surface could affect the density of states at the surface and the density states perturbed by substrate are imaged. Further study is required to understand this moiré pattern of MoS_2 on Cu(111).

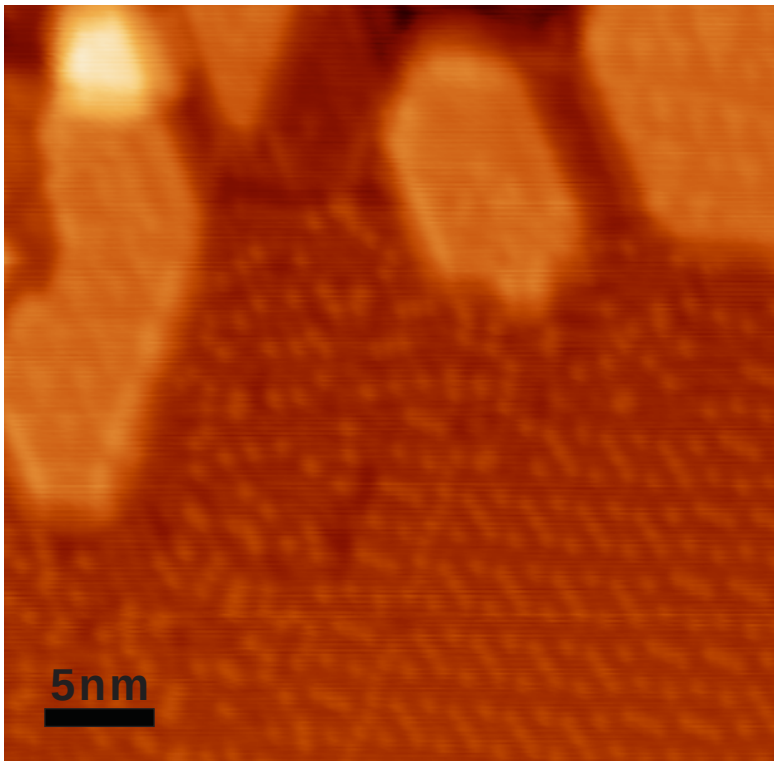

Figure 8.3 An STM image of single layer MoS_2 clusters formed repeated deposition of sulfur and molybdenum with a new pattern of sulfur near MoS_2 clusters.

8.3 Conclusion

We presented a new method that uses a liquid sulfur source, benzenethiol, instead of gas, to form disulfided molybdenum clusters on the 2D surface. Well ordered monolayer of molybdenum disulfide was synthesized by repeated deposition of sulfur and molybdenum in an alternating fashion. This idea and experimental procedures can be

developed for thr industrial purposes; yet, further study is required in order to understand the growth mode and control of the process.

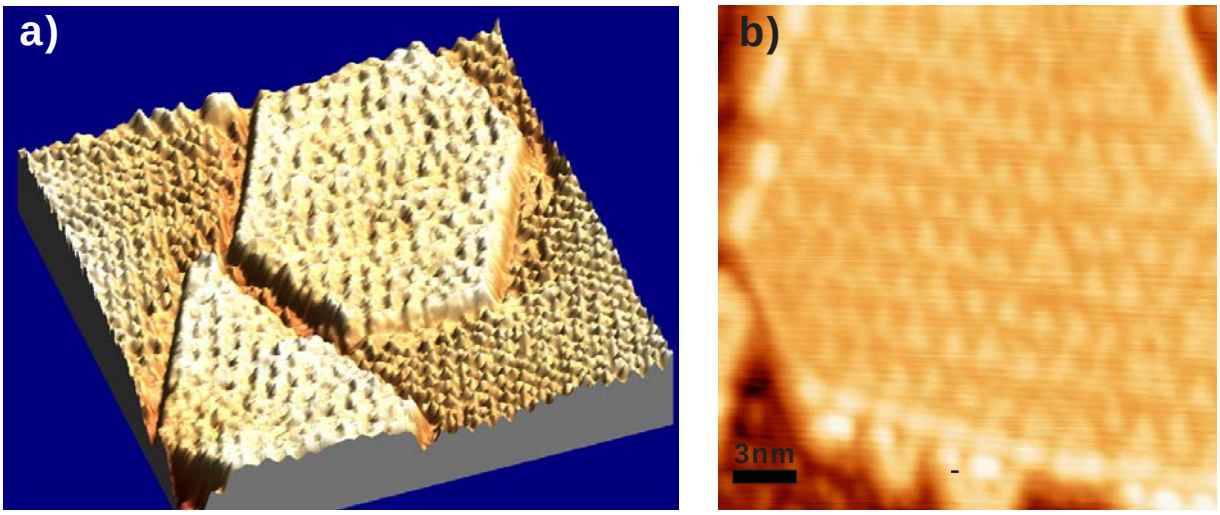

Figure 8.4 a) 3D rendered STM image of single layer MoS_2 on S/Cu(111) and b) high resolution 2D STM image STM of the top of single layer MoS_2.

References

1. Binnig, G. and H. Rohrer, *Scanning tunneling Microscopy.* Helvetica Physica Acta, 1982. **55**(6): p. 726-735.

2. Eigler, D.M. and E.K. Schweizer, *POSITIONING SINGLE ATOMS WITH A SCANNING TUNNELING MICROSCOPE.* Nature, 1990. **344**(6266): p. 524-526.

3. Pawin, G., Molecular diffusion, energetics, and structures on Cu(111) as studied by scanning tunneling microscopy 2008, UC, Riverside: Riverside. p. 97.

4. Kwon, K.Y., Reactivity, dynamics, and film formation of arenethiols studied by STM, in Disseration. 2005, UC, Riverside: Riverside. p. 136.

5. Kresse, G. and J. Hafner, *Ab initio molecular dynamics of liquid metals.* Physical Review B: Condensed Matter and Materials Physics, 1993. **47**(1): p. 558-61.

6. Perdew, J.P. and Y. Wang, ACCURATE AND SIMPLE ANALYTIC REPRESENTATION OF THE ELECTRON-GAS CORRELATION-ENERGY. Physical Review B, 1992. **45**(23): p. 13244-13249.

7. Payne, M.C., et al., Iterative minimization techniques for ab initio total-energy calculations: molecular dynamics and conjugate gradients. Reviews of Modern Physics, 1992. **64**(4): p. 1045-97.

8. Schlickum, U., et al., *Metal-organic honeycomb nanomeshes with tunable cavity size.* Nano Letters, 2007. **7**(12): p. 3813-3817.

9. Schickum, U., et al., *Metal-organic honeycomb nanomeshes with tunable cavity size.* Nano Letters, 2007. **7**(12): p. 3813-3817.

10. Yaghi, O.M., et al., *Reticular synthesis and the design of new materials.* Nature, 2003. **423**(6941): p. 705-714.

11. Ruben, M., et al., *Grid-type metal ion architectures: Functional metallosupramolecular arrays.* Angewandte Chemie-International Edition, 2004. **43**(28): p. 3644-3662.

12. Dmitriev, A., et al., *Modular assembly of two-dimensional metal-organic coordination networks at a metal surface.* Angewandte Chemie-International Edition, 2003. **42**(23): p. 2670-2673.

13. Barth, J.V., G. Costantini, and K. Kern, *Engineering atomic and molecular nanostructures at surfaces.* Nature, 2005. **437**(7059): p. 671-679.

14. Zhu, N., T. Osada, and T. Komeda, *Supramolecular assembly of biphenyl dicarboxylic acid on Au(1 1 1).* Surface Science, 2007. **601**(8): p. 1789-1794.

15. Tait, S.L., et al., *Metal-organic coordination interactions in Fe-Terephthalic acid networks on Cu(100).* Journal of the American Chemical Society, 2008. **130**(6): p. 2108-2113.

16. Classen, T., et al., *Hydrogen and coordination bonding supramolecular structures of trimesic acid on Cu(110).* Journal of Physical Chemistry A, 2007. **111**(49): p. 12589-12603.

17. Breitruck, A., et al., *Interaction of Cu atoms with ordered 2D oligopyridine networks.* Surface Science, 2007. **601**(18): p. 4200-4205.

18. Zhang, H.M., et al., One-step preparation of large-scale self-assembled monolayers of cyanuric acid and melamine supramolecular species on Au(111) surfaces. Journal of Physical Chemistry C, 2008. **112**(11): p. 4209-4218.

19. Stepanow, S., et al., Surface-assisted assembly of 2D metal-organic networks that exhibit unusual threefold coordination symmetry. Angewandte Chemie-International Edition, 2007. **46**(5): p. 710-713.

20. Seitsonen, A.P., et al., Density functional theory analysis of carboxylate-bridged diiron units in two-dimensional metal-organic grids. Journal of the American Chemical Society, 2006. **128**(17): p. 5634-5635.

21. Vanderbilt, D., Soft Self-Consistent Pseudopotentials in a Generalized Eigenvalue Formalism. Physical Review B, 1990. **41**(11): p. 7892-7895.

22. Monkhorst, H.J. and J.D. Pack, *SPECIAL POINTS FOR BRILLOUIN-ZONE INTEGRATIONS.* Physical Review B, 1976. **13**(12): p. 5188-5192.

23. Wu, X., et al., Towards extending the applicability of density functional theory to weakly bound systems. Journal of Chemical Physics, 2001. **115**(19): p. 8748-8757.

24. Wong, K.L., et al., *A Molecule Carrier.* Science, 2007. **315**: p. 1391-1393.

25. Kwon, K.Y., et al., Unidirectional adsorbate motion on a high-symmetry surface: "Walking" molecules can stay the course. Physical Review Letters, 2005. **95**(16): p. 166101.

26. Pawin, G., et al., *A Quantitative Approach to Hydrogen Bonding at a Metal Surface.* JOURNAL OF THE AMERICAN CHEMICAL SOCIETY, 2007. **129**: p. 12056 -12057.

27. Pawin, G., et al., *A homomolecular porous network at a Cu(111) surface.* Science, 2006. **313**(5789): p. 961-962.

28. Pawin, G., et al., *A Quantitative Approach to Hydrogen Bonding at a Metal Surface.* Journal of the American Chemical Society, 2007. **129**(40): p. 12056-12057.

29. Kroger, J., et al., *Molecular orbital shift of perylenetetracarboxylic-dianhydride on gold.* Chemical Physics Letters, 2007. **438**(4-6): p. 249-253.

30. Venkataraman, D., et al., *A coordination geometry table of the d-block elements and their ions.* Journal of Chemical Education, 1997. **74**(8): p. 915-918.

31. Pretsch, T., I. Brudgam, and H. Hartl, *Synthesis and crystal structure of [N(Hex)(4)](infinity)(3)[Cu-2(CN)(3)].* Zeitschrift Fur Anorganische Und Allgemeine Chemie, 2003. **629**(6): p. 942-944.

32. Ghosh, C., A. Kara, and T. Rahman, *Theoretical aspects of vertical and lateral manipulation of atoms.* Surface Science, 2002. **502**: p. 519-526.

33. *Spartan 06*, Wavefunction Inc.: Irvine, CA.

34. Chretien, S. and H. Metiu, Density functional study of the charge on Au-n clusters (n=1-7) supported on a partially reduced rutile TiO2(110): Are all clusters negatively charged? Journal of Chemical Physics, 2007. **126**(10): p. 7.

35. Worz, A.S., et al., Charging of Au atoms on TiO2 thin films from CO vibrational spectroscopy and DFT calculations. Journal of Physical Chemistry B, 2005. **109**(39): p. 18418-18426.

36. Chen, F., et al., *Measurement of single-molecule conductance.* Annual Review of Physical Chemistry, 2007. **58**: p. 535-564.

37. Heath, J.R. and M.A. Ratner, *Molecular electronics.* Physics Today, 2003. **56**(5): p. 43-49.

38. Dimitrakopoulos, C.D. and P.R.L. Malenfant, *Organic thin film transistors for large area electronics.* Advanced Materials, 2002. **14**(2): p. 99-103.

39. Love, J.C., et al., Self-assembled monolayers of thiolates on metals as a form of nanotechnology. Chemical Reviews, 2005. **105**(4): p. 1103-1169.

40. Poirier, G.E., Characterization of organosulfur molecular monolayers on Au(111) using scanning tunneling microscopy. Chemical Reviews, 1997. **97**(4): p. 1117-1127.

41. Theobald, J.A., et al., Controlling molecular deposition and layer structure with supramolecular surface assemblies. Nature, 2003. **424**(6952): p. 1029-1031.

42. Xu, B., et al., *Coverage dependent supramolecular structures: C_{60} : ACA monolayers on Ag(111).* Journal of the American Chemical Society, 2006. **128**(26): p. 8493-8499.

43. Llanes-Pallas, A., et al., Trimodular engineering of linear supramolecular miniatures on Ag(111) surfaces controlled by complementary triple hydrogen bonds. Angewandte Chemie-International Edition, 2008. **47**(40): p. 7726-7730.

44. Otero, R., et al., *Guanine quartet networks stabilized by cooperative hydrogen bonds.* Angewandte Chemie-International Edition, 2005. **44**(15): p. 2270-2275.

45. Lackinger, M., et al., Dynamics of grain boundaries in two-dimensional hydrogen-bonded molecular networks. Small, 2005. **1**(5): p. 532-539.

46. De Feyter, S. and F.C. De Schryver, *Two-dimensional supramolecular self-assembly probed by scanning tunneling microscopy.* Chemical Society Reviews, 2003. **32**(3): p. 139-150.

47. Keeling, D.L., et al., Assembly and processing of hydrogen bond induced supramolecular nanostructures. Nano Letters, 2003. **3**(1): p. 9-12.

48. Weckesser, J., et al., Mesoscopic correlation of supramolecular chirality in one-dimensional hydrogen-bonded assemblies. Physical Review Letters, 2001. **8709**(9): p. art. no.-096101.

49. Barth, J.V., et al., *Building supramolecular nanostructures at surfaces by hydrogen bonding.* Angewandte Chemie-International Edition, 2000. **39**(7): p. 1230-1234.

50. Nakagawa, T., H. Tanaka, and T. Kawai, Two-dimensional self-assembly of uracil molecules on Cu(111) surfaces: A low-temperature STM study. Surface Science, 1997. **370**(1): p. L144-L148.

51. Payer, D., et al., Ionic Hydrogen Bonds Controlling Two-Dimensional Supramolecular Systems at a Metal Surface. Chemistry - A European Journal, 2007. **13**(14): p. 3900-3906.

52. Zhang, X., et al., Effect of C-H ... F and O-H ... O hydrogen bonding in forming self-assembled monolayers of BF2-substituted beta-dicarbonyl derivatives on HOPG: STM investigation. Journal of Physical Chemistry C, 2007. **111**(37): p. 13851-13854.

53. Rohde, D., C.J. Yan, and L.J. Wan, C-H ...F hydrogen bonding: The origin of the self-assemblies of bis(2,2 '-difluoro-1,3,2-dioxaborine). Langmuir, 2006. **22**(10): p. 4750-4757.

54. Desiraju, G.R., *Hydrogen bridges in crystal engineering: Interactions without borders.* Accounts of Chemical Research, 2002. **35**(7): p. 565-573.

55. Desiraju, G.R., C-H center dot center dot center dot O and other weak hydrogen bonds. From crystal engineering to virtual screening. Chemical Communications, 2005(24): p. 2995-3001.

56. Yokoyama, T., et al., Selective assembly on a surface of supramolecular aggregates with controlled size and shape. Nature, 2001. **413**(6856): p. 619-621.

57. Barth, J.V., et al., Scanning Tunneling Microscopy Observations on the Reconstructed Au(111) Surface - Atomic-Structure, Long-Range Superstructure, Rotational Domains, and Surface-Defects. Physical Review B, 1990. **42**(15): p. 9307-9318.

58. Muller, T., et al., *Ultra-high vacuum scanning tunneling microscopy and theoretical studies of 1-halohexane monolayers on graphite.* Proceedings of the National Academy of Sciences of the United States of America, 2005. **102**(15): p. 5315-5322.

59. Wong, K., et al., *Effect of halo substitution on the geometry of arenethiol films on Cu(111).* Journal of the American Chemical Society, 2004. **126**(25): p. 7762-7763.

60. Kresse, G. and J. Hafner, *Abinitio Molecular-Dynamics for Liquid-Metals.* Physical Review B, 1993. **47**(1): p. 558-561.

61. Payne, M.C., et al., Iterative Minimization Techniques for Abinitio Total-Energy Calculations - Molecular-Dynamics and Conjugate Gradients. Reviews of Modern Physics, 1992. **64**(4): p. 1045-1097.

62. Jadzinsky, P.D., et al., Structure of a thiol monolayer-protected gold nanoparticle at 1.1 angstrom resolution. Science, 2007. **318**(5849): p. 430-433.

63. Maksymovych, P. and J.T. Yates, *Au adatoms in self-assembly of benzenethiol on the Au(111) surface.* Journal of the American Chemical Society, 2008. **130**(24): p. 7518-7519.

64. Rao, B., et al., *Measurement of a Linear Free Energy Relationship One Molecule at a Time.* Proceedings of the National Academy of Sciences of the United States of America, 2004. **101**(52): p. 17920.

65. Wong, K., K.Y. Kwon, and L. Bartels, *Surface Dynamics of Benzenethiol Molecules.* Applied Physics Letters, 2006. **88**: p. 183106.

66. Prins, L.J., D.N. Reinhoudt, and P. Timmerman, *Noncovalent synthesis using hydrogen bonding.* Angewandte Chemie-International Edition, 2001. **40**(13): p. 2383-2426.

67. Barrena, E., C. Ocal, and M. Salmeron, Evolution of the structure and mechanical stability of self-assembled alkanethiol islands on Au(111) due to diffusion and ripening. Journal of Chemical Physics, 1999. **111**(21): p. 9797-9802.

68. Morgenstern, K., et al., *Measurement of energies controlling ripening and annealing on metal surfaces.* Physical Review Letters, 1998. **80**(3): p. 556-559.

69. Bohringer, M., et al., *Two-dimensional self-assembly of magic supramolecular clusters.* JOURNAL OF PHYSICS-CONDENSED MATTER, 1999. **11**(49): p. 9871-9878.

70. Gimzewski, J.K., et al., *Rotation of a single molecule within a supramolecular bearing.* Science, 1998. **281**(5376): p. 531-533.

71. Shirai, Y., et al., *Directional control in thermally driven single-molecule nanocars.* Nano Letters, 2005. **5**(11): p. 2330-2334.

72. Kelly, T.R., H. De Silva, and R.A. Silva, *Unidirectional rotary motion in a molecular system.* Nature, 1999. **401**(6749): p. 150-152.

73. v. Delius, M., E.M. Geertsema, and D.A. Leigh, *A synthetic small molecule that can walk down a track.* Nature Chemistry, 2009. **2**: p. 96-101.

74. Moore, J.S., *Shape-persistent molecular architectures of nanoscale dimension.* Accounts of Chemical Research, 1997. **30**(10): p. 402-413.

75. Baber, A.E., H.L. Tierney, and E.C.H. Sykes, *A Quantitative Single-Molecule Study of Thioether Molecular Rotors.* Acs Nano, 2008. **2**(11): p. 2385-2391.

76. Vaughan, O.P.H., et al., *A chemically switchable molecular pinwheel.* Angewandte Chemie-International Edition, 2006. **45**(23): p. 3779-3781.

77. Balzani, V., et al., *Artificial Molecular Machines.* Angew. Chem. Int. Ed., 2000. **39**: p. 3348 - 3391.

78. Horch, S., et al., Enhancement of surface self-diffusion of platinum atoms by adsorbed hydrogen. NATURE, 1999. **398**(6723): p. 134-136.

79. Grill, L., et al., *Rolling a single molecular wheel at the atomic scale.* Nature Nanotechnology, 2007. **2**(2): p. 95-98.

80. Kottas, G.S., et al., *Artificial molecular rotors.* Chemical Reviews, 2005. **105**(4): p. 1281-1376.

81. van Delden, R.A., et al., *Unidirectional molecular motor on a gold surface.* Nature, 2005. **437**(7063): p. 1337-1340.

82. Kay, E.R., D.A. Leigh, and F. Zerbetto, *Synthetic molecular motors and mechanical machines.* Angewandte Chemie-International Edition, 2007. **46**(1-2): p. 72-191.

83. Liu, Y., et al., *Linear artificial molecular muscles.* Journal of the American Chemical Society, 2005. **127**(27): p. 9745-9759.

84. Wong, K.L., et al., *Coverage and nearest-neighbor dependence of adsorbate diffusion.* Journal of Chemical Physics, 2005. **123**(20): p. 201102.

85. Heinrich, A., et al., *Molecule cascades.* SCIENCE, 2002. **298**(5597): p. 1381-1387.

86. Briner, B., et al., Microscopic molecular diffusion enhanced by adsorbate interactions. SCIENCE, 1997. **278**(5336): p. 257-260.

87. Fischer, B., et al., *Nucleation kinetics on inhomogeneous substrates: Al/Au(111).* Physical Review Letters, 1999. **82**(8): p. 1732-1735.

88. Meyer, W. and H. Neldel, Concerning the relationship between the energy constant epsilon and the quantum constant alpha in the conduction-temperature formula in oxydising semi-conductors. Physikalische Zeitschrift, 1937. **38**: p. 1014-1019.

89. Boisvert, G., L.J. Lewis, and A. Yelon, *Many-Body Nature of the Meyer-Neldel Compensation Law for Diffusion.* Physical Review Letters, 1995. **75**(3): p. 469-472.

90. Fisher, D.J., ed. *Defect and Diffusion Forum: The Meyer-Neldel Rule*. Vol. 192-193. 2001, Trans Tech Pulbications Inc.: Zurich (Switzerland).

91. Berland, K., T.L. Einstein, and P. Hyldgaard, *Rings sliding on a honeycomb network: Adsorption contours, interactions,and assembly of benzene on Cu(111).* Physical Review B (Condensed Matter and Materials Physics), 2009. **80**: p. 155431.

92. Mercurio, G., et al., Structure and Energetics of Azobenzene on Ag(111): Benchmarking Semiempirical Dispersion Correction Approaches. Physical Review Letters, 2010. **104**(3): p. -.

93. Kua, J., et al., Direct comparisons of rates for low temperature diffusion of hydrogen and deuterium on Cu(001) from quantum mechanical calculations and scanning tunneling microscopy experiments. Journal of Chemical Physics, 2001. **115**(12): p. 5620-5624.

94. Lauhon, L. and W. Ho, Direct observation of the quantum tunneling of single hydrogen atoms with a scanning tunneling microscope. Physical Review Letters, 2000. **85**(21): p. 4566-4569.

95. Price, P.J., *Attempt frequency in tunneling.* American Journal of Physics, 1998. **66**(12): p. 1119-1122.

96. Witte, G., et al., *Oxygen-induced reconstructions on Cu(211).* Physical Review B, 1998. **58**(19): p. 13224-13232.

97. Haruta, M., et al., Novel Gold Catalysts for the Oxidation of Carbon-Monoxide at a Temperature Far Below 0-Degrees-C. Chemistry Letters, 1987(2): p. 405-408.

98. Chen, M.S. and D.W. Goodman, *The structure of catalytically active gold on titania.* Science, 2004. **306**(5694): p. 252-255.

99. Somorjai, G.A., *Introduction to surface chemistry and catalysis*. 1994, New York: Wiley. xxiv, 667 p.

100. Mantooth, B.A., et al., Analyzing the motion of benzene on Au{111}: Single molecule statistics from scanning probe images. Journal of Physical Chemistry C, 2007. **111**(17): p. 6167-6182.

101. Han, P., et al., *Benzene on Au (111) at 4 K: Monolayer growth and tip-induced molecular cascades.* Journal of the American Chemical Society, 2004. **126**(34): p. 10787-10793.

102. Sachs, C., et al., Spatiotemporal self-organization in a surface reaction: From the atomic to the mesoscopic scale. SCIENCE, 2001. **293**(5535): p. 1635-1638.

103. Hendriksen, B., S. Bobaru, and J. Frenken, *Oscillatory CO oxidation on Pd(100) studied with in situ scanning tunneling microscopy.* Surface Science, 2004. **552**(1-3): p. 229-242.

104. Tierney, H.L., A.E. Baber, and E.C.H. Sykes, *Atomic-Scale Imaging and Electronic Structure Determination of Catalytic Sites on Pd/Cu Near Surface Alloys.* Journal of Physical Chemistry C, 2009. **113**(17): p. 7246-7250.

105. Mitsui, T., et al., *Diffusion and pair interactions of CO molecules on Pd(111).* Physical Review Letters, 2005. **94**(3): p. 036101.

106. Longwitz, S., et al., High-coverage structures of carbon monoxide adsorbed on Pt(111) studied by high-pressure scanning tunneling microscopy. JOURNAL OF PHYSICAL CHEMISTRY B, 2004. **108**(38): p. 14497-14502.

107. Kulawik, M., et al., *Interaction of CO molecules with surface state electrons on Ag(111).* Surface Science, 2005. **590**(2-3): p. L253-L258.

108. Stepanow, S., et al., Steering molecular organization and host-guest interactions using two-dimensional nanoporous coordination systems. NATURE MATERIALS, 2004. **3**(4): p. 229-233.

109. Decker, R., et al., Using metal-organic templates to steer the growth of Fe and Co nanoclusters. Applied Physics Letters, 2008. **93**(24): p. 243102.

110. Berner, S., et al., *Boron nitride nanomesh: Functionality from a corrugated monolayer.* Angewandte Chemie-International Edition, 2007. **46**(27): p. 5115-5119.

111. Bartels, L., *Tailoring molecular layers at metal surfaces.* Nature Chemistry, 2010. **2**(2): p. 87-95.

112. Otero, R., et al., Nanostructuring Cu surfaces using custom-designed molecular molds. NANO LETTERS, 2004. **4**(1): p. 75-78.

113. Static Confinement of CO in much larger edge-pits has been investigated by Kulawik et al., Surf. Sci. 590, L53 (2005)

114. Bartels, L., G. Meyer, and K. Rieder, Controlled vertical manipulation of single CO molecules with the scanning tunneling microscope: A route to chemical contrast. Applied Physics Letters, 1997. **71**(2): p. 213-215.

115. Bartels, L., G. Meyer, and K. Rieder, The evolution of CO adsorption on Cu(111) as studied with bare and CO-functionalized scanning tunneling tips. Surface Science, 1999. **432**(3): p. L621-L626.

116. Repp, J., et al., Substrate mediated long-range oscillatory interaction between adatoms: Cu/Cu(111). Physical Review Letters, 2000. **85**(14): p. 2981-2984.

117. Shan, B., et al., *Coverage-Dependent CO Adsorption Energy from First-Principles Calculations.* Journal of Physical Chemistry C, 2009. **113**(15): p. 6088-6092.

118. Heller, E., et al., Scatterin and Adsorption of Surface Electron Waves in Quantum Corrals. NATURE, 1994. **369**(6480): p. 464-466.

119. Fiete, G.A. and E.J. Heller, *Colloquium: Theory of quantum corrals and quantum mirages.* Reviews of Modern Physics, 2003. **75**(3): p. 933-948.

120. Lobo-Checa, J., et al., Band Formation from Coupled Quantum Dots Formed by a Nanoporous Network on a Copper Surface. SCIENCE, 2009. **325**(5938): p. 300-303.

121. Hyldgaard, P. and T.L. Einstein, *Surface-state mediated three-adsorbate interaction.* Europhysics Letters, 2002. **59**(2): p. 265-271.

122. Haruta, M., *Catalysis - Gold rush.* Nature, 2005. **437**(7062): p. 1098-1099.

123. Rastei, M.V., et al., *Size-dependent surface states of strained cobalt nanoislands on Cu(111).* Physical Review Letters, 2007. **99**(24): p. -.

124. Gsell, M., P. Jakob, and D. Menzel, *Effect of substrate strain on adsorption.* Science, 1998. **280**(5364): p. 717-720.

125. Stranick, S.J., M.M. Kamna, and P.S. Weiss, *Atomic-Scale Dynamics of a 2-Dimensional Gas-Solid Interface.* Science, 1994. **266**(5182): p. 99-102.

126. Negulyaev, N.N., et al., Direct Evidence for the Effect of Quantum Confinement of Surface-State Electrons on Atomic Diffusion. Physical Review Letters, 2008. **101**(22): p. -.

127. Sykes, E., et al., Substrate-mediated interactions and intermolecular forces between molecules adsorbed on surfaces. Accounts of Chemical Research, 2003. **36**(12): p. 945-953.

128. Nanayakkara, S.U., et al., Long-Range Electronic Interactions at a High Temperature: Bromine Adatom Islands on Cu(111). Physical Review Letters, 2007. **98**(20): p. 206108-4.

129. Lukas, S., G. Witte, and C. Woll, Novel mechanism for molecular self-assembly on metal substrates: Unidirectional rows of pentacene on Cu(110) produced by a substrate-mediated repulsion. Physical Review Letters, 2002. **88**(2): p. 028301

130. Einstein, T.L., Interactions between adsorbate particles, in Physical structure of solid surfaces, Handbook of surface science ; v. 1, W.N. Unertl, Editor. 1996, Elsevier: Amsterdam ; New York. p. 577-650.

131. Fichthorn, K. and M. Scheffler, *Island nucleation in thin-film epitaxy: A first-principles investigation.* Physical Review Letters, 2000. **84**(23): p. 5371-5374.

132. Österlund, L., et al., *Quantitative determination of adsorbate-adsorbate interactions.* Physical Review Letters, 1999. **83**(23): p. 4812-4815.

133. Stepanyuk, V., et al., Quantum interference and long-range adsorbate-adsorbate interactions. Physical Review B, 2003. **68**(20): p. -.

134. Bogicevic, A., et al., *Nature, strength, and consequences of indirect adsorbate interactions on metals.* Physical Review Letters, 2000. **85**(9): p. 1910-1913.

135. Mathews, J. and R.L. Walker, *Mathematical methods of physics*. 2d ed. 1970, New York,: W. A. Benjamin.

136. Gross, L., et al., *Scattering of surface state electrons at large organic molecules.* Physical Review Letters, 2004. **93**(5): p. 056103.

137. Atkinson, K.E. and W. Han, *Elementary numerical analysis*. 3rd ed. 2004, Hoboken, NJ: J. Wiley & Sons.

138. Kiełbasiński, A. and H. Schwetlick, *Numerische lineare Algebra : eine computerorientierte Einführung*. 1988, Thun [etc.]: Harri Deutsch. 472 S.

139. Kevan, S.D. and R.H. Gaylord, High-Resolution Photoemission-Study of the Electronic-Structure of the Noble-Metal (111) Surfaces. PHYSICAL REVIEW B, 1987. **36**(11): p. 5809-5818.

140. Burgi, L., et al., *Noble metal surface states: deviations from parabolic dispersion.* SURFACE SCIENCE, 2000. **447**(1-3): p. L157-L161.

141. Jaeger, C., *Rock mechanics and engineering*. 2d ed. 1979, Cambridge [Eng.] ; New York: Cambridge University Press. xii, 523 p.

142. Fujita, Y., N.A. Duncan, and J.C. Lotz, *Radial tensile properties of the lumbar annulus fibrosus are site and degeneration dependent.* Journal of Orthopaedic Research, 1997. **15**(6): p. 814-819.

143. Weber, M., R. Koch, and K. Rieder, UHV Cantilever beam technique for quantitative measurements of magnetization, magnetistriction, and intrinsic stress of ultrathin magnetic films. Physical Review Letters, 1994. **73**(8): p. 1166-1169.

144. Ibach, H., The role of surface stress in reconstruction, epitaxial growth and stabilization of mesoscopic structures. Surface Science Reports, 1997. **29**(5-6): p. 195-263.

145. Muller, P. and A. Saul, *Elastic effects on surface physics.* Surface Science Reports, 2004. **54**(5-8): p. 157-258.

146. France, C.B., et al., Scanning tunneling microscopy study of the coverage-dependent structures of pentacene on Au(111). Langmuir, 2003. **19**(4): p. 1274-1281.

147. Wan, L.J. and K. Itaya, In situ scanning tunnelling microscopy of benzene, naphthalene, and anthracene adsorbed on Cu(111) in solution. Langmuir, 1997. **13**(26): p. 7173-7179.

148. Witte, G. and C. Woll, Growth of aromatic molecules on solid substrates for applications in organic electronics. Journal of Materials Research, 2004. **19**(7): p. 1889-1916.

149. Ample, F. and C. Joachim, *A semi-empirical study of polyacene molecules adsorbed on a Cu(110) surface.* Surface Science, 2006. **600**(16): p. 3243-3251.

150. Lukas, S., et al., Adsorption of acenes on flat and vicinal Cu(111) surfaces: Step induced formation of lateral order. Journal of Chemical Physics, 2001. **114**(22): p. 10123-10130.

151. Bilic, A., et al., *Adsorption of benzene on copper, silver, and gold surfaces.* Journal of Chemical Theory and Computation, 2006. **2**(4): p. 1093-1105.

152. Dion, M., et al., *Van der Waals density functional for general geometries.* Physical Review Letters, 2004. **92**(24): p. 246401.

153. Chakarova-Käck, S.D., et al., Application of van der Waals density functional to an extended system: Adsorption of benzene and naphthalene on graphite. Physical Review Letters, 2006. **96**(14): p. 146107.

154. Chakarova-Käck, S.D., et al., Binding of polycyclic aromatic hydrocarbons and graphene dimers in density functional theory. New Journal of Physics, 2010. **12**: p. 013017.

155. Hammer, B., L.B. Hansen, and J.K. Norskov, Improved adsorption energetics within density-functional theory using revised Perdew-Burke-Ernzerhof functionals. Physical Review B, 1999. **59**(11): p. 7413-7421.

156. Blochl, P.E., O. Jepsen, and O.K. Andersen, *Improved Tetrahedron Method for Brillouin-Zone Integrations.* Physical Review B, 1994. **49**(23): p. 16223-16233.

157. Mortensen, J.J., L.B. Hansen, and K.W. Jacobsen, *Real-space grid implementation of the projector augmented wave method.* Physical Review B, 2005. **71**(3): p. 035109.

158. Narayan, V., N. Menon, and S. Ramaswamy, *Nonequilibrium steady states in a vibrated-rod monolayer: tetratic, nematic, and smectic correlations.* Journal of Statistical Mechanics-Theory and Experiment, 2006: p. P01005.

159. Bates, M.A. and D. Frenkel, *Phase behavior of two-dimensional hard rod fluids.* Journal of Chemical Physics, 2000. **112**(22): p. 10034-10041.

160. Simmons, G. and H. Wang, *Single crystal elastic constants and calculated aggregate properties: a handbook*. 2d ed. 1971, Cambridge, Mass.: M.I.T. Press. xv, 370 p.

161. Novoselov, K.S., et al., *Two-dimensional atomic crystals.* Proceedings of the National Academy of Sciences of the United States of America, 2005. **102**(30): p. 10451-10453.

162. Geim, A.K. and K.S. Novoselov, *The rise of graphene.* Nature Materials, 2007. **6**(3): p. 183-191.

163. Bolotin, K.I., et al., *Ultrahigh electron mobility in suspended graphene.* Solid State Communications, 2008. **146**(9-10): p. 351-355.

164. Balandin, A.A., et al., *Superior Thermal Conductivity of Single-Layer Graphene.* Nano Letters, 2008. **8**(3): p. 902-907.

165. Ghosh, S., et al., Extremely high thermal conductivity of graphene: Prospects for thermal management applications in nanoelectronic circuits. Applied Physics Letters, 2008. **92**(15): p. 3.

166. Chen, Z., et al., *Graphene nano-ribbon electronics.* Physica E: Low-dimensional Systems and Nanostructures, 2007. **40**(2): p. 228-232.

167. Wang, X., et al., Room-Temperature All-Semiconducting Sub-10-nm Graphene Nanoribbon Field-Effect Transistors. Physical Review Letters, 2008. **100**(20): p. 206803.

168. Berger, C., et al., Ultrathin Epitaxial Graphite: 2D Electron Gas Properties and a Route toward Graphene-based Nanoelectronics. The Journal of Physical Chemistry B, 2004. **108**(52): p. 19912-19916.

169. Geim, A.K. and K.S. Novoselov, *The rise of graphene.* Nat Mater, 2007. **6**(3): p. 183-191.

170. Meric, I., et al., Current saturation in zero-bandgap, top-gated graphene field-effect transistors. Nat Nano, 2008. **3**(11): p. 654-659.

171. Lee, C., et al., Anomalous Lattice Vibrations of Single- and Few-Layer MoS2. ACS Nano, 2010. **4**(5): p. 2695-2700.

172. Mak, K.F., et al., *Atomically Thin MoS_{2}: A New Direct-Gap Semiconductor.* Physical Review Letters, 2010. **105**(13): p. 136805.

173. Helveg, S., et al., *Atomic-scale structure of single-layer MoS2 nanoclusters.* Physical Review Letters, 2000. **84**(5): p. 951-954.

174. Wong, K.L., et al., *Halogen-Substituted Thiophenol Molecules on Cu(111).* Langmuir, 2004. **20**(25): p. 10928-10934.

175. Wahlstrom, E., et al., Observation of ordered structures for S/Cu(111) at low temperature and coverage. Physical Review B, 1999. **60**(15): p. 10699.

176. Wahlstrom, E., et al., *Low-temperature structure of S/Cu(111).* Physical Review B, 2001. **64**(15): p. 155406.

177. Ruan, L., et al., A scanning tunneling microscopy study of the interaction of S with the Cu(111) surface. Ultramicroscopy, 1992. **42-44**(Part 1): p. 498-504.

178. H. Topsøe, B.S.C., and F. E. Massoth, *Hydrotreating Catalysis, Science and Technology*. 1996: Springer-Verlag.

179. Tersoff, J. and D.R. Hamann, *Theory of the scanning tunneling microscope.* PHYSICAL REVIEW B, 1985. **31**(2): p. 805.

180. Sutter, E., P. Albrecht, and P. Sutter, *Graphene growth on polycrystalline Ru thin films.* Applied Physics Letters, 2009. **95**(13).

181. Cheng, Z.H., et al., Adsorbates in a Box: Titration of Substrate Electronic States. Physical Review Letters. **105**(6).

182. Wintterlin, J. and M.L. Bocquet, *Graphene on metal surfaces.* Surface Science, 2009. **603**(10-12): p. 1841-1852.

183. Xhie, J., et al., *Giant and supergiant lattices on graphite.* PHYSICAL REVIEW B, 1993. **47**(23): p. 15835.

184. Rong, Z.Y., Extended modifications of electronic structures caused by defects: Scanning tunneling microscopy of graphite. PHYSICAL REVIEW B, 1994. **50**(3): p. 1839.

185. Cee, V.J., D.L. Patrick, and T.P. Beebe, *Unusual aspects of superperiodic features on highly oriented pyrolytic graphite.* SURFACE SCIENCE, 1995. **329**(1-2): p. 141-148.

186. Rong, Z.Y. and P. Kuiper, Electronic effects in scanning tunneling microscopy: Moiré pattern on a graphite surface. PHYSICAL REVIEW B, 1993. **48**(23): p. 17427.

187. Kuwabara, M., D.R. Clarke, and D.A. Smith, *ANOMALOUS SUPERPERIODICITY IN SCANNING TUNNELING MICROSCOPE IMAGES OF GRAPHITE.* APPLIED PHYSICS LETTERS, 1990. **56**(24): p. 2396-2398.

188. Ohuchi, F.S., et al., *VANDERWAALS EPITAXIAL-GROWTH AND CHARACTERIZATION OF MOSE2 THIN-FILMS ON SNS2.* Journal of Applied Physics, 1990. **68**(5): p. 2168-2175.

189. Parkinson, B.A., et al., PERIODIC LATTICE-DISTORTIONS AS A RESULT OF LATTICE MISMATCH IN EPITAXIAL-FILMS OF 2-DIMENSIONAL MATERIALS. APPLIED PHYSICS LETTERS, 1991. **58**(5): p. 472-474.